Energy Geoscience 6 (2025) 100461

Contents lists available at ScienceDirect

Energy Geoscience

journal homepage: www.keaipublishing.com/en/journals/energy-geoscience

Reservoir characterization and well production proxy analyses on drill cuttings: Case study from the Flysch play in the Vienna Basin (NE Austria)

Jasemin A. Ölmez [a,b,*], Benjamin Busch [a], Rolf Möbius [c], Kanchan Dasgupta [c], Albert L. Gauer [c], Filippo Tosoratti [c], Christoph Hilgers [a,b]

[a] Institute of Applied Geosciences, Structural Geology & Tectonics, Karlsruhe Institute of Technology, Adenauerring 20a, 76131, Karlsruhe, Germany
[b] KIT Campus Transfer GmbH, TTE Reservoir-Geology, Haid-und-Neu-Straße 7, 76131, Karlsruhe, Germany
[c] OMV Exploration & Production GmbH, Trabrennstrasse 6-8, 1020, Vienna, Austria

ARTICLE INFO

Article history:
Received 17 February 2025
Received in revised form
18 June 2025
Accepted 13 August 2025

Handling Editor: A.E. Radwan

Keywords:
Drill cuttings
Vienna Basin
Flysch
Glauconite sandstone
Diagenesis

ABSTRACT

Drill cuttings, though rarely used, are crucial subsurface samples to understand petrographic properties affecting reservoir quality. Unlike core material, cuttings are continuously available along the wellbore and can be used during drilling to monitor progress. Therefore, cuttings may allow a semi-quantitative, statistical calibration of rock properties from the subsurface, but they are often underutilized. Although fracture and vein orientations cannot be reconstructed from drill cuttings, the presence of veins and their internal textures (open, partially sealed or sealed) in specific formation sections and depths can be identified and analyzed using e.g., transmitted light microscopy and cathodoluminescence to supplement characterization at the well site and subsequently assess production behavior. Borehole gamma ray logs in combination with handheld portable X-ray fluorescence (pXRF) analyses on cleaned and dried drill cuttings can be used to further improve the depth accuracy of the cutting samples and to geochemically fingerprint the samples, based on the Si/Al ratio, as a proxy for sandstone-rich and mudrock-rich sections of the well. In this study, eighty-three sandstone cutting samples from two wells, covering ~400 m of stratigraphy targeting the Paleocene-Eocene Greifenstein Fm. equivalent (Glauconite Sandstone, GLS) in the Vienna Basin (Austria), were studied. They also cover parts of three different reservoir sections (1. to 3. GLS). The Flysch play in the Vienna Basin hosts several sandstone-mudrock interbeds and is composed of several nappes, forming complex reservoir compartments. The glauconite contents vary between different sections of the GLS, where the highest is observed in the 3. GLS. The sandstones are predominantly cemented by ferroan calcite, resulting in low optical porosity (<5 %) in both wells, with only individually elevated porosity, related to partially dissolved K-feldspar grains. A paragenetic sequence solely based on cuttings further highlights that reservoir quality in the studied section is independent of sandstone compaction, but is related to lower optical porosity in finer-grained sandstones and higher carbonate vein cement contents. Furthermore, productive intervals are related to lower Fe + Mg contents. The understanding of reservoir properties, diagenesis, and their influence on fluid flow is crucial for successful exploration and reduction of uncertainty in reservoir production and development. The diagenetic variations from cuttings and the geochemical fingerprint by pXRF are linked to reservoir quality and production performance of individual well perforations. This approach can provide additional information on reservoir quality where core material is unavailable.

1. Introduction

Reservoir assessment and a better understanding of reservoir quality variations are critically important for successful exploration, reduction of uncertainties and help to understand the

* Corresponding author. Institute of Applied Geosciences, Structural Geology & Tectonics, Karlsruhe Institute of Technology, Adenauerring 20a, 76131, Karlsruhe, Germany.
E-mail address: jasemin.oelmez@kit.edu (J.A. Ölmez).
Peer review under the responsibility of Editorial Board of Energy Geoscience.

https://doi.org/10.1016/j.engeos.2025.100461

economic viability of natural resources (e.g., Ozkan et al., 2011; Camp et al., 2018; Worden et al., 2018; Ciriaco et al., 2020). Reservoir quality assessment therefore is of importance particularly for exploration and production of hydrocarbons or geothermal water in areas with increasingly challenging conditions.

While drilling a well, drill cuttings are the first opportunity to directly analyze the subsurface rocks on-site, though these are only rock fragments and have undergone damage by the drilling process. Furthermore, drill cuttings are the only geological samples in oil, gas or geothermal wells that are usually continuously taken and can provide direct information on rock properties such as the mineralogy of detrital grains, authigenic cementation, vein composition and optical porosity. Drill cuttings are used to assess formation properties and to improve the drilling performance in an inexpensive way (e.g., Tiainen et al., 2002) and have been integrated with gamma ray and other borehole measurements to better assess reservoir characteristics (e.g., Gulf of Suez Rift, Radwan, 2022). The potential of drill cuttings to better understand the reservoir performance or source potential was assessed e.g., for fields in the Vienna Basin of Austria (Rupprecht et al., 2017), the Volga-Ural Basin in Russia (Ibrahem and Morozov, 2024), the Montney tight gas siltstone play in Canada (Sanei et al., 2020), and at onshore blocks in the Sultanate of Oman (Swami et al., 2022).

Geochemical fingerprinting is based on several geochemical techniques as e.g., fluid inclusion techniques, light stable isotope analyses or C-O clumped isotopes to analyze diagenetic or sedimentary features (Worden et al., 2018; Mamdouh et al., 2024). However, mineralogical analyses of core samples or cuttings is often performed using laboratory X-ray diffraction (e.g., Gier et al., 2018), infrared techniques and point counting using a microscope (Worden et al., 2018). Chemical analysis on core or cutting samples is used less, but can be performed using e.g., benchtop X-ray fluorescence and portable X-ray fluorescence (pXRF) devices (Worden et al., 2018). The pXRF analyzer provides low-cost, rapidly available data of both cleaned core and cutting material and is used for e.g., chemostratigraphy and detection of trace metal contaminants in aquifers (e.g., Zambito et al., 2022). Results of pXRF measurements of geothermal drill cuttings have been shown to be comparable in accuracy with laboratory XRF results for many elements, especially elements with atomic numbers >17 (Mauriohooho et al., 2016). Being a non-destructive method, pXRF allows to reuse the cuttings for petrographic analysis. Alternative works utilizing drill cuttings in industry approaches shown by Swami et al. (2022) and by Pandion Energy in Norway (Offshore, 2021) are employing automated mineralogy mapping techniques using a SEM platform. However, sample preparation and analysis is time consuming and ultimately lags behind drilling operations. Therefore, linking pXRF measurements to cuttings on the well site and calibrating the process to standard petrographic workflows may enable the use of pXRF measurements to assess likely producing intervals in future wells. Caja et al. (2019) also described the combination of petrography and geochemistry methods for analysing cutting material using virtual microscopy, automated mineralogy and digital petrophysics.

In general, the primary composition of sandstones is controlled by factors such as the provenance and plate tectonics (e.g., Dickinson and Suczek, 1979), the depositional system, transport energy, transport distance (e.g., Bjørrlykke, 1998; Lupin and Hampson, 2020) and therefore grain size and sorting, which can affect reservoir properties (e.g., Coskun et al., 1993; Griffiths et al., 2019). However, diagenetic processes such as compaction and cementation or dissolution can overprint primary sedimentary controls on reservoir properties, resulting in either improvement or reduction of given matrix permeability and porosity of the reservoir rock (e.g., Bjørlykke, 1988; Coskun et al., 1993; Dutton and Loucks, 2010; Morad et al., 2010; Busch et al., 2024). Quartz cement can either result in reduction of pore space and therefore the deterioration of reservoir quality (e.g., Bjørlykke and Egeberg, 1993; Morad et al., 2010) or in preservation and stabilizing of the framework and pore space (if not filling the pore space completely), improving the reservoir quality (Molenaar, 1986; Makowitz et al., 2006; Busch et al., 2022). Furthermore, in tight rocks, natural fractures play an important role for reservoir exploitation as they are the main fluid conduit (besides faults) (e.g., Olson et al., 2009; Bahrami et al., 2012; Khelifa et al., 2014). Whilst all these are established from core, and outcrop analyses, our motivation was to test if some of these correlations can be also recognized on drill cuttings.

In the study area, the Upper Cretaceous to Paleocene Flysch play is assessed, as it is interpreted as a fractured reservoir play leading to the fact that exploration and production wells commonly deliver mixed results. As fractures are commonly present in the investigated sections (Möbius et al., 2023), fracture and vein characteristics are likely to influence reservoir quality and productivity. Cores are not continuously available, therefore cuttings were used to better understand the influence of petrographic properties. An in-depth assessment of vein cement textures was undertaken to better assess their influence on reservoir quality. Therefore, the petrography, diagenesis and geochemical fingerprint of sandstone drill cuttings from reservoir rocks from two wells are presented in this study. Detailed petrographic studies will provide a paragenetic sequence for this reservoir section based on cuttings only.

The Flysch play in the Vienna Basin, Austria, was already discovered to be prolific to produce oil and gas since the beginning of the 20th century. Production volumes peaked in the 1940s, however the area is still actively producing. Furthermore, detailed structural diagenetic assessments on veins and partially sealed fractures will shed light on the effect of fractures in the reservoir section of the lithology. The geochemical fingerprint measured with a portable X-ray fluorescence analyzer (pXRF) is used in combination with petrographic data obtained from thin sections and borehole gamma ray (GR) logs. By comparison with information on producing and non-producing intervals, possible proxies from pXRF data for reservoir quality assessments were derived. Such proxies may be used directly on the wellsite. Using geochemical proxies based on pXRF analyses may close that time-gap from analyses such as SEM-based automated mineralogy mapping techniques, as cuttings can be already washed and dried directly at the wellsite for their description. The presented pXRF approach, if calibrated to standard reservoir quality analyses, may thus enable the assessment of suitable reservoir quality intervals directly on the well site. It can therefore be used to accelerate completion and perforation decisions, influence well continuation and data acquisition needs and thus may reduce total well cost. Furthermore, such a calibration can be similarly applied on historic cuttings of intervals that were not of interest at the time of drilling (e.g., dry holes in the hydrocarbon industry). However, such may meanwhile be of interest for geothermal development or to evaluate the quality of subsurface storage locations.

2. Geological setting and tectonic evolution

The Vienna Basin, a major hydrocarbon province in Central Europe (Fig. 1a), is a NE-SW-trending, 200 km long and up to 60 km wide, Tertiary thin-skinned intramontane pull-apart basin in Austria, Czech Republic and Slovakia (Ladwein, 1988; Piller et al., 1996; Arzmüller et al., 2006; Strauss et al., 2006; Rupprecht et al.,

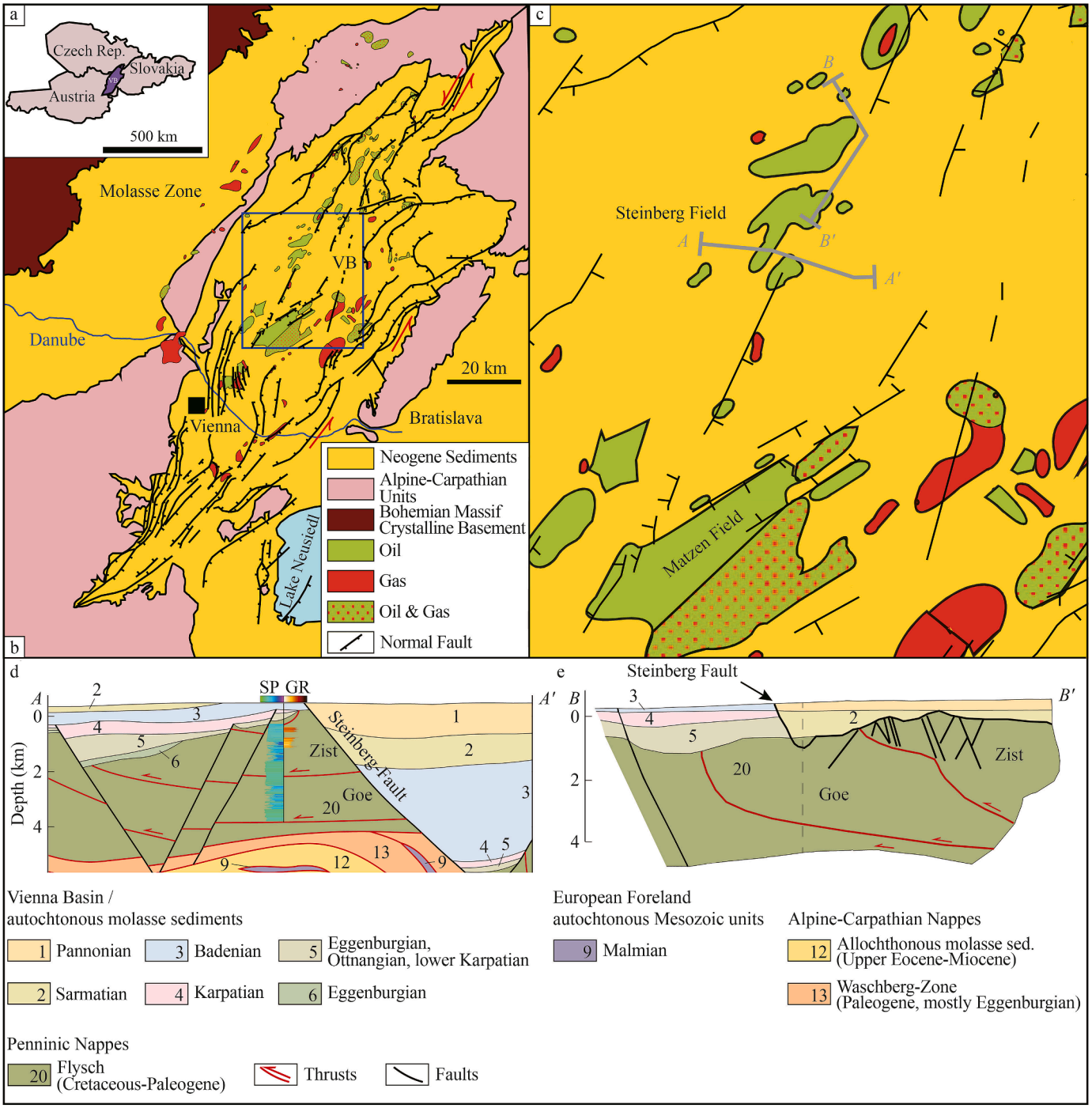

Fig. 1. Location and profiles of the Vienna Basin. (a) Location of the Vienna Basin (VB) in the NE part of Austria, SE part of the Czech Republic and W part of Slovakia redrawn from Rupprecht et al. (2018). (b) Overview map of prominent units and the regional geology of the Vienna Basin, redrawn & modified from Rupprecht et al. (2018) and references therein. Vienna is marked with a black rectangle. Oil (green), gas (red) and oil & gas (green with red dots) fields adapted from Arzmüller et al. (2006), the study area is marked with a blue box. (c) Magnification of the blue box in b) showing the study area and marked profiles in d) and e). (d) Simplified W-E profile along the line *A*-*A*′ with early thrusts and later normal and strike-slip faults, highlighting the Zistersdorf (Zist) and Gösting (Goe) units (redrawn and modified after Berka, 2015). Spontaneous potential (SP) log (purple low, green high) is available for the whole Zis and Goe units, whereas gamma ray log data (GR) is in historic wells often only available for intervals of particular interest (reference well provided by OMV). (e) NW-SE to NE-SW profile along *B*-*B*′ with interpreted lithological sequence for 3 to 5 (redrawn and modified after Wessely, 2006). The vertical dashed line indicates the change of orientation of the profile (parallel to the Steinberg fault from dashed line to *B*′).

2017). It is part of the Neogene Paratethys Basin System and forms a structural evolution along the junction of the Eastern Alps in the West, the southeast Pannonian Basin System and the Western Carpathians in the NE (Royden et al., 1985; Wagreich and Schmid, 2002). The basin hosts crystalline basement rocks from the Bohemian Massif, Mesozoic autochthonous sediments and foreland basin deposits from the Cenozoic, and a Neogene clastic basin fill (Fig. 1b) (Ladwein, 1988; Rupprecht et al., 2017). During Alpine subduction of the European lithosphere, thrusting occurred and led to the deposition of flysch in the Carpathian foredeep (Royden

et al., 1985). The flysch is composed of submarine sediment-flows to turbidity currents (e.g., Rammel, 1989 and references therein). The basin locally hosts Alpine thrust sheets of Cretaceous to Miocene flysch, as well as subordinate molasse deposits (Fig. 1c) (Royden et al., 1985). Neogene sedimentary rocks of the Vienna Basin are sandstones, marls and subordinate carbonates, which can exceed thicknesses up to 5000 m in the depocenters (Ladwein, 1988; Gier et al., 2008). At the base of the Neogene part of the section, Late Burdigalian sediments were deposited in a fluvial to lacustrine environment (Piller et al., 1996; Gier et al., 2008). In the Early Badenian, a marine transgression started and evolved to brackish conditions during the Sarmatian (Piller et al., 1996; Gier et al., 2008). The decrease in salinity leads to the deposition of fluvial to lacustrine deposits in the Pannonian (Piller et al., 1996; Gier et al., 2008, and references therein). The Vienna Basin was separated into fault blocks during the pull-apart phase, which may have resulted in local variations in sedimentary evolution (Strauss et al., 2006).

Strike-slip faulting, back-arc extension and retreating subduction led to the formation of Miocene pull-apart basins in the Alps such as the Vienna Basin (Royden et al., 1985; Decker, 1996; Decker et al., 2005). The Vienna Basin started to form as a piggy-back basin along a sinistral fault system during the Early Miocene, and continued evolution as a rhombic shaped pull-apart basin until the Late Miocene when W-E compression started, which also led to regional basin inversion (Royden et al., 1985; Decker, 1996). From the Pleistocene to recent time W-E extension started (Decker, 1996).

One of the main tectonic units of the flysch in Austria (Wienerwald Flysch, Cretaceous-Eocene) and also the northernmost is the Greifenstein Nappe, containing the Altlengbach Fm. (Upper Cretaceous), Glauconite Sandstone Series (Paleocene-Eocene) and Steinberg Flysch (Eocene) (Götzinger et al., 1954; Rammel, 1989; Mattern and Wang, 2008) (Fig. 2a). The Greifenstein Nappe itself is subdivided into the Gösting and Zistersdorf units, separated by internal thrusts, leading to a stacking of Upper Cretaceous to Eocene lithologies (Fig. 2b) (Götzinger et al., 1954; Rammel, 1989). This stacking is supported by biostratigraphic studies (Wessely, 2006 and references therein), and the repetition of log responses (two sections of low SP response in Fig. 1d, GR in Fig. 2b).

2.1. Reservoir system

Exploration for oil and gas in the Vienna Basin started around 150 years ago and first economically producible discoveries of conventional oil and gas fields in the flysch were made in the early 1930s (Arzmüller et al., 2006; Rupprecht et al., 2017; Möbius et al., 2023). About 6000 wells have been drilled there since the 20th century (Arzmüller et al., 2006) and the Vienna Basin is a well-studied area in terms of the stratigraphic history and depositional settings (see Harzhauser et al., 2020 and references therein). Although the source rock is well known (e.g., Schulz et al., 2010; Rupprecht et al., 2017; Schicker et al., 2021), the reservoir rock properties in sandstone reservoirs in the Flysch play of the Vienna Basin is not fully understood due to the small-scale reservoir compartmentalization and the lack of comprehensive modern data within the flysch. Furthermore, only few studies highlight and focus on the impact of diagenesis on the reservoir quality in other sandstone units of the Vienna Basin (e.g., Gier et al., 2008). The two studied legacy wells captured the Greifenstein Fm. equivalent Glauconite Sandstone (GLS, Zistersdorf unit) in the flysch of the Vienna Basin. Production from the 1. and 2. GLS (Paleogene) and the 3. GLS (Upper Cretaceous) are restricted to the footwall of the Steinberg Fault and hanging wall of the Hochleiten–Pirawarth faults (cf. Sachsenhofer et al., 2025 and references therein). The dominant hydrocarbon source rocks in the Vienna Basin are mudstones from the autochthonous Malmian Mikulov Fm. (e.g., Rupprecht et al., 2017; Sachsenhofer et al., 2025). The marly limestones from the Falkenstein Fm., which show a thickness of more than 1 km and overlie the crystalline rocks of the Bohemian Massif, and the Middle Jurassic Gresten Group additionally show source potential (Piller et al., 1996; Rupprecht, 2017; Rupprecht et al., 2017; Schicker et al., 2021; Sachsenhofer et al., 2025). The flysch reservoir is sealed by interlayering mudstones and overlain by the Miocene reservoir formation (Sachsenhofer et al., 2025). Hydrocarbon migration is interpreted as pre-Miocene to Miocene, and likely follows basal flysch overthrusts (Rupprecht, 2017). The Malmian Mikulov Fm. may also host a significant shale gas/shale oil potential besides the important role for conventional oil and gas (Schulz et al., 2010).

Generally, the flysch in the Vienna Basin represents a sandstone reservoir rock with poor matrix porosities which can only locally reach up to a maximum of 15 % porosity and with generally low matrix permeabilities, often below 0.1×10^{-3} μm^2 (Möbius et al., 2023). Reduced permeability values are interpreted due to quartz cementation and glauconitic clay mineral content (Sauer et al., 1992). Predictive and reliable controls on reservoir quality are not established. This leads to a challenge for well planning, as finding high reservoir quality intervals with open or partially sealed fractures, which can only partially be resolved by seismic data, is complex (Möbius et al., 2023). As the reservoir contains stacked producing intervals with thicknesses from 5 to 20 m (Fig. 2b) distributed along the wellbore and core runs do not exceed 20 m, they are unlikely to allow the study of reservoir quality controls. However, as cuttings are continuously sampled along the whole well (Fig. 2b), the assessment may unlock a better understanding of the distribution of producing and non-producing intervals.

3. Materials and methods

For this study, eighty-three cutting samples covering an interval of ~400 m stratigraphy were collected from two wells targeting the Paleocene-Eocene Glauconite Sandstone (GLS, Greifenstein Fm. equivalent) of the Vienna Basin. Well 1 covers 22 samples from the 1. GLS (depth: 1190–1235 m) and 2. GLS (depth: 1275–1295 m), covering a total depth range of 105 m. Well 2 covers 61 samples from the 1. GLS (depth: 930–995 m), 2. GLS (depth: 1035–1095 m), and 3. GLS (depth: 1100–1270 m) covering a total depth range of 340 m. The lateral distance of the two wells is less than 1 km. Cuttings in the present wells were regularly sampled (every 2.5, 5.0, or 7.5 m), however, the provided cutting samples are not representing a single depth, but likely represent a depth interval. Here, we interpreted the cuttings to represent an average rock composition of the respective 2.5, 5.0, or 7.5 m interval (for specific depths, see supplementary material). This accounts for the possible mixing of cutting material happening during the drilling process, therefore the described cuttings are treated as average composition for a well section as also noticed by e.g., Traineau et al. (1991). Furthermore, claystones/mudstones and soft siltstones can be disaggregated and fine sand can be entrained in the drilling mud.

The provided samples of rock chips are between 25 g and 50 g. The samples were placed into a plastic cup, cleaned with tap water, then placed into an ultrasonic bath for maximum durations of 30 s in order to remove residual drilling mud. No disaggregation of cuttings or removal of depositional clay mineral matrix was observed when compared with thin section samples from core material. In addition to remaining drilling mud residue, this step removed metal shavings as well as wood remnants from the

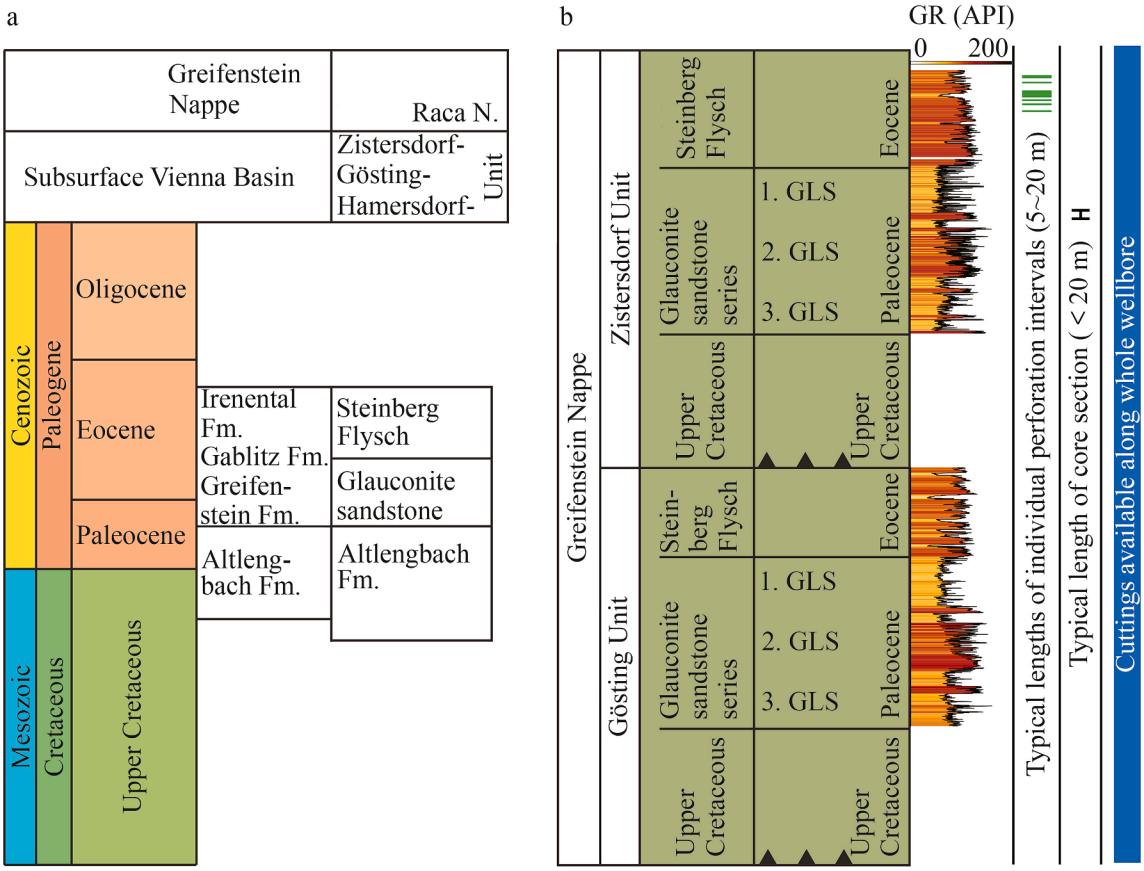

Fig. 2. Regional stratigraphy. (a) Simplified stratigraphy of the Vienna Basin Flysch, modified after Wessely (2006) and references therein, colors are adapted from the international chronostratigraphic table by Cohen et al. (2024). (b) Simplified subdivision of the Greifenstein Nappe including 1. to 3. GLS (Glauconite Sandstone), thrusting results in repetition of lithologies, modified after Wessely (2006) and references therein. Colors for the flysch (Cretaceous to Paleogene) are related to the profile in Fig. 1d for Zistersdorf and Gösting unit. GR well log data provided by OMV is given for the studied sections, showing similar log responses. Due to thrusts, layer doubling of sandstone and mudstone units are shown in the GR from reference/example wells, were the Greifenstein equivalent was continuously logged. The typical thickness of single production perforations is between 5 m and 20 m, whereas the typical length of a core section is < 20 m, but cuttings are available along the whole section (blue field).

wooden storage boxes. As all cutting samples were equally cleaned using this process, petrographic and geochemical data are comparable within this dataset. The cleaned cuttings were dried in a vacuum-oven at 40 °C for at least three to four days until weight constancy was achieved. Samples are subsequently documented photographically using an Optika SZN-4 binocular microscope with a mounted Jenoptik Progres Gryphax Subra camera (Fig. 3).

3.1. Portable X-ray fluorescence (pXRF) and gamma ray (GR) well log

Elemental concentrations of drill cuttings were determined using a Bruker S1Titan800 pXRF operating with an electric power of 4 W, an electric current of max. 200 μA, and a voltage of max. 50 kV in GeoExploration mode, which can measure elements from Mg to U. The device is composed of a Rh-target X-ray tube, an Ultralene window and a Graphene window silicon drift detector. As pXRF measurements are non-destructive, they are preferred for the analyses of small amounts of samples, which should also be studied petrographically. The reproducibility using standards delivered with the pXRF device is shown by Quandt et al. (2024).

The bulk rock geochemistry measurements were performed on 83 rock cutting samples after cleaning and drying but before selecting cuttings for petrographic analyses. The rock chips were placed in a ceramic bowl for measurement. Each sample was measured three times for 20 s (cf. Quandt et al., 2024). Concentrations of Si, Al, Fe, Ca, K, S, Ti, Mn, Sr, Zr, Ba, Ni, Cu, Zn, Rb, Y, Nb and Pb were measured in this study. Element concentrations showing an average for the individual well below 0.01 wt% are classified as trace elements. For comparison with the gamma ray well log trends, the Si/Al ratio is determined from the pXRF measurements (see Craigie, 2018). As the provided cutting samples are mostly taken in a 5 m interval, the provided gamma ray log data provided by the operator was also averaged (arithmetic mean) over 5 m intervals to better compare it to the average rock compositions. Where the gamma ray value is increasing, a decrease in the Si/Al value is expected, and vice versa.

3.2. Petrography

Sandstone cuttings were picked from the bulk cutting samples using the binocular microscope for subsequent thin section preparation and further diagenetic studies and the assessment of optical porosity. Different sizes of cuttings were combined to reflect the distribution of each sample bag. In addition, sandstone and mudstone cuttings containing veins and individual vein fragments were preferentially sampled to enable studying the vein paragenesis and fracture porosity of the fractured sandstone reservoir. Fracture porosity is restricted to intragranular fractures, as these are also observed in thin sections from core material. Whereas most uncemented intergranular fractures are interpreted to be induced by drilling, as they are absent in thin sections from core material. The

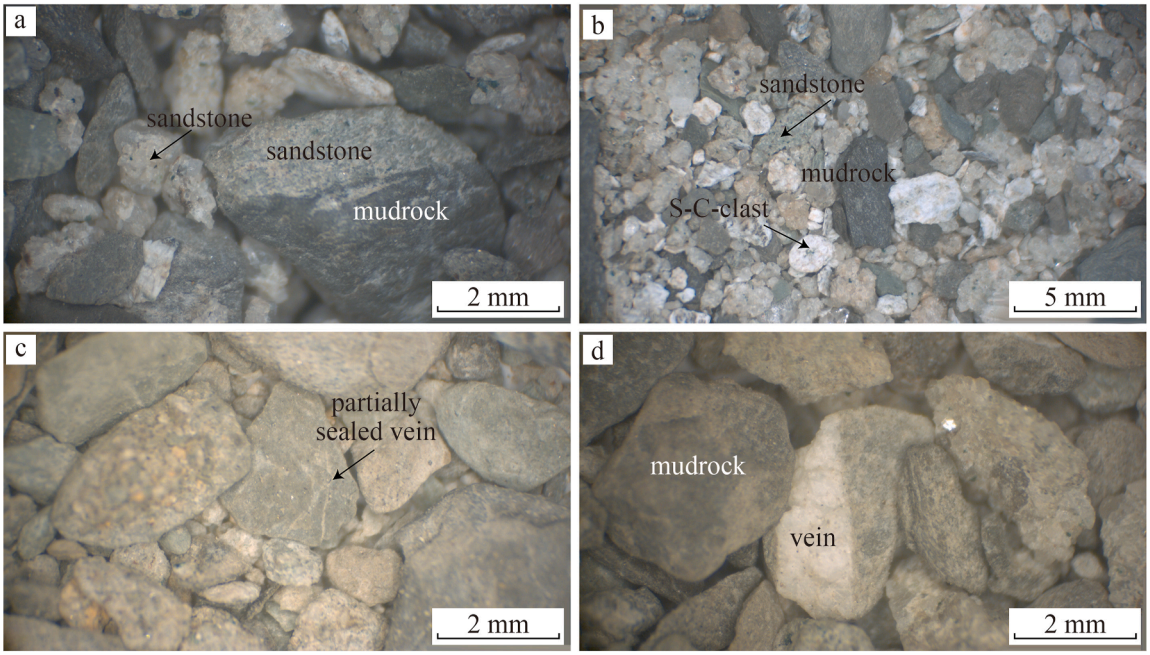

Fig. 3. Photographs of individual cuttings from wells 1 & 2. (a) Fine grained sandstone-mudrock transition (well 1, depth 1215 m). (b) Sandstone and mudrock cuttings with white ground-up host rock clasts showing S-C-shear structure (S-C-clast) in thin sections (well 1, depth 1220 m). (c) Partially sealed vein in mudrock cutting (well 2, depth 940 m). (d) Mudrock and sandstone cuttings with a vein penetrating a cutting (well 2, depth 960 m).

selected drill cuttings were then embedded in blue-dyed epoxy to enable the optical determination of porosity and were prepared to a thickness of 30 μm for thin section analysis. Of total eighty-three thin sections prepared, sixty-nine were stained with Alizarin Red S and potassium ferricyanide in 0.3 % HCl to distinguish different carbonate phases according to Dickson (1965) and covered with a glass cover slip. Therefore, calcite stains pale pink to red, ferroan calcite royal blue to purple or mauve, ferroan dolomite pale to deep turquoise whereas dolomite remains colorless (Dickson, 1965). Additional fourteen thin sections were polished and analyzed using cold cathode cathodoluminescence (CITL CL8200 Mk5-2 Optical Cathodoluminescence System mounted on a Leica DIALUX 20 ES) (e.g., Monsees et al., 2020b) at an acceleration voltage of 10.3 kV and a current of 325 μA. The luminescence of carbonates is influenced by the amount of Mn or Fe (Budd et al., 2000). A bright orange luminescence is mostly related to Mn-enrichment, whereas a darker luminescence may indicate a higher amount of Fe (Budd et al., 2000).

Grain sizes were analyzed on each thin section from sandstone cuttings using thin section microphotographs and ImageJ. Therefore, a grid adjusted to the maximum grain size of each sample was applied to the images and the long axis of at least 100 grains in each sample were measured to obtain area-weighted results (e.g., Busch et al., 2018). The arithmetic mean is given as the grain size per sample. Grain size thresholds are taken from Folk (1980) with size classes after Wentworth (1922). Sorting was calculated according to Folk and Ward (1957). Rock composition was analyzed using a semi-automatic Pelcon point counting stage installed on a Leica DMLP transmitted light microscope. For each sample, 300 points were counted with a step-length adjusted to the maximum grain sizes (supplementary material) (e.g., Quandt et al., 2024). The point counting only covers the cuttings, whereas the blue dyed epoxy resin and non-sandstone grains in between sandstone cuttings mounted on the same slide are skipped. Point counted categories are based on the Touchstone™ point counting scheme (Busch et al., 2018). The differentiation between glauconite “sensu stricto” and other glauconitic minerals (Odin and Fullagar, 1988) is not possible using transmitted light microscopy. Therefore, the term glauconite to describe most likely detrital green grains showing different shaped pellets, but the same interference color under crossed polarizers is used here. Glauconite can have several origins and the genesis of glauconite is still under debate (e.g., Triplehorn, 1966; Odin and Fullagar, 1988; López-Quirós et al., 2020; Wilmsen et al., 2024). From point counts detrital quartz (Q), feldspar (F) and rock fragments (R) were normalized and plotted in the QFR diagram after Folk (1980). However, as an individual thin section made from cuttings may contain sandstone cuttings of different rock types, the presented QFR compositions may not accurately represent individual beds, but changes along the studied well sections may still be assessed. Optical porosity was obtained from point counting and differentiated in intergranular, intragranular porosity (in K-feldspar, carbonate or undifferentiated rock fragments), and fracture porosity. Microporosity present in e.g., clay minerals and chlorite cannot be point counted using transmitted light microscopy (e.g., Nadeau and Hurst, 1991). The intergranular volume (*IGV*) was calculated based on point counting results and represents the sum of intergranular pore space ($P_{\text{intergranular}}$), depositional clay mineral matrix ($M_{\text{depositional}}$), and intergranular cements ($C_{\text{intergranular}}$) and indicates the degree of compaction (Paxton et al., 2002). Similar to the QFR composition, derived *IGV* does not represent individual rock types, but may show variation along the studied well sections.

4. Results

4.1. pXRF

The main geochemical elements for well 1 and well 2 are Si (avg.: 22.87 wt% and 14.59 wt%), Al (avg.: 4.27 wt% and 2.36 wt%), Ca (1.71 wt% and 2.14 wt%), K (avg.: 0.97 wt% and 0.82 wt%), and Fe (avg.: 1.87 wt% and 1.51 wt%) (Fig. 4). Trace elements for both wells are S, Ti, Mn, Sr, Zr, Ba, Ni, Cu, Zn, Rb, Y, Nb, and Pb (supplementary material). Si contents in well 1 are higher than in well 2 (Fig. 5a),

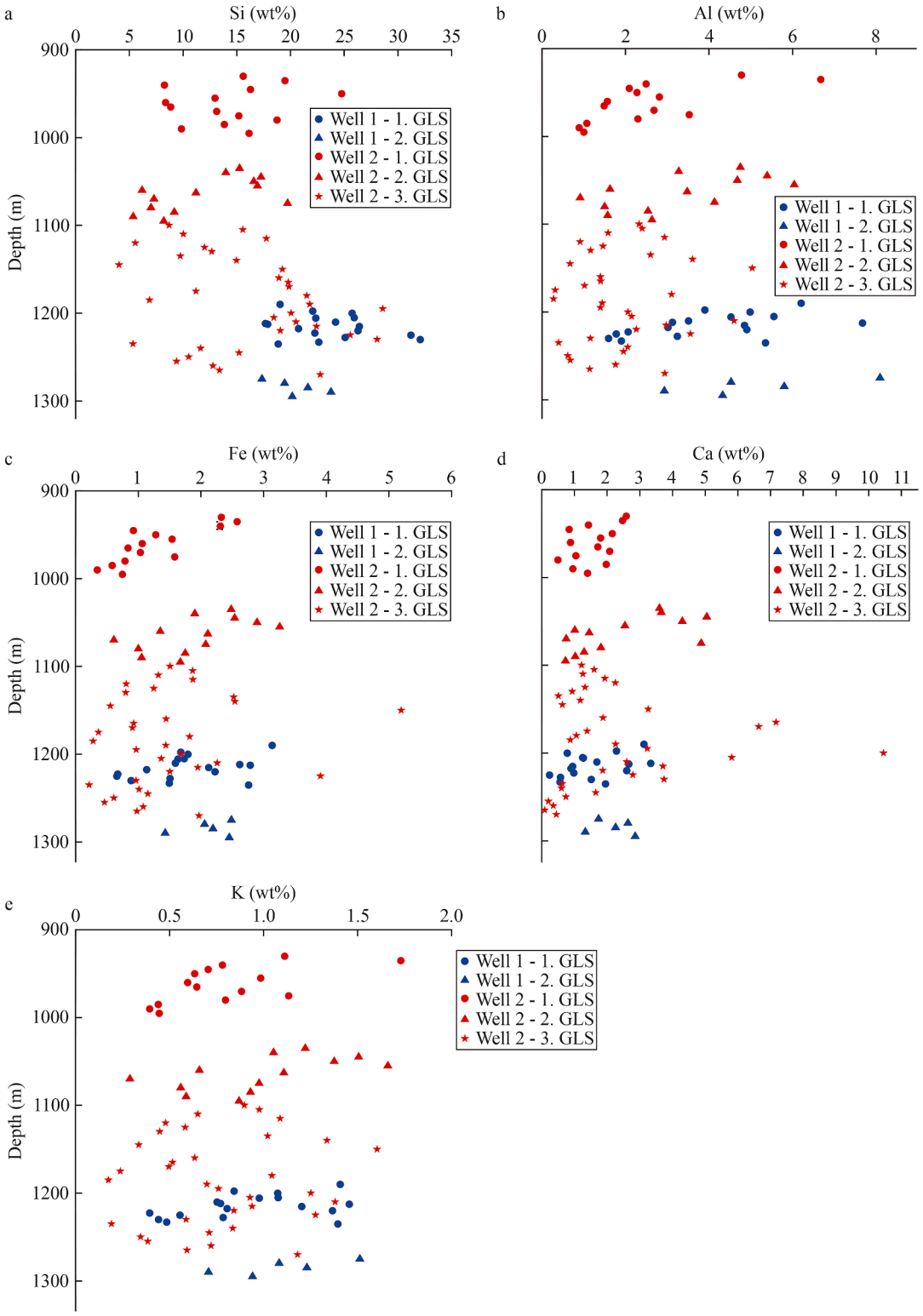

Fig. 4. The main geochemical components. For well 1 (blue) and well 2 (red) the main geochemical components are (a) Si, (b) Al, (c) Fe, (d) Ca, and (e) K. The samples cover different GLS, which are shown as circles (1. GLS), triangles (2. GLS) and stars (3. GLS).

whereas the other elements do not show any trend within well depth and GLS subdivision. Higher Ca contents are recorded only within a section from 1160 m to 1210 m in the 3. GLS of well 2 and related to higher contents of carbonate rock fragments and calcitic bioclasts (Fig. 4d).

4.2. Borehole gamma ray data and correlation to Si/Al bulk rock ratio

The provided gamma ray data for well 1 originate from well depth 1185 m–1295 m and range between 42 API and 143 API. The

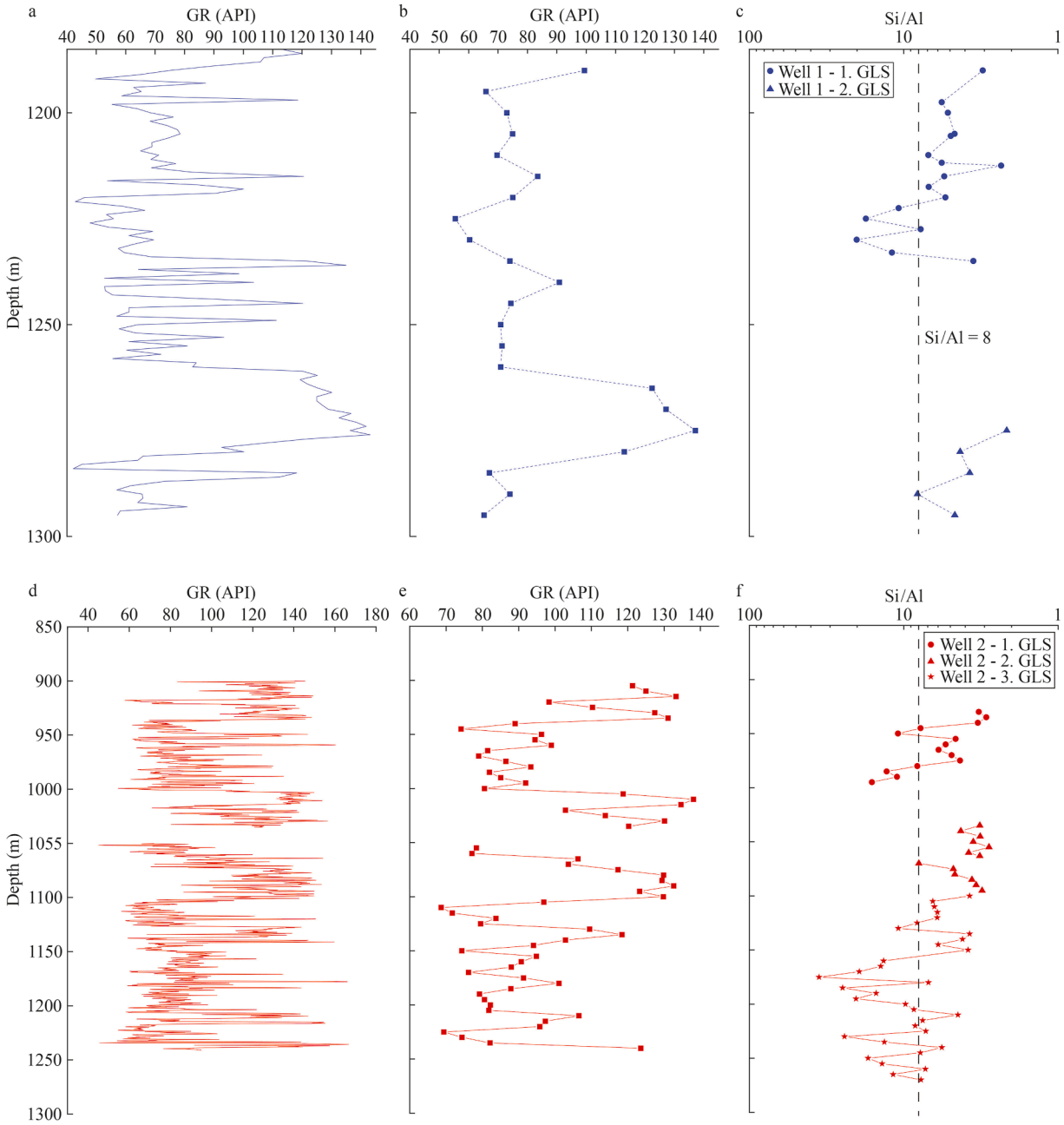

Fig. 5. Gamma Ray well log and Si/Al ratio. Log GR data in API for well 1 (a) and well 2 (d), arithmetic mean of GR data in API in 5 m intervals for well 1 (b) and well 2 (e), and Si/Al ratio observed from bulk drill cuttings from well 1 (c) and well 2 (f). Note that the Si/Al axis is inverted to more easily compare trends, circles represent samples from 1. GLS, triangles 2. GLS, and stars 3. GLS. Si/Al values of >8 in (c) and (f) are indicative for non-argillaceous sandstones (dashed line as sandstone cut off) after Craigie (2018).

data for well 2 originate from well depth 900 m–1241 m and range between 45 API and 166 API. The 5 m-averages (arithmetic mean) for the gamma ray log from well 1 range from 55 API to 137 API, and for well 2 from 68 API to 138 API. The Si/Al ratio for well 1 vary between 2.1 and 20.1, and for well 2 between 2.8 and 35.3. Both GR and Si/Al data vary with well depth. On average, higher Si/Al ratios and lower GR values are found in the 1. and 3. GLS and lower Si/Al showing higher GR values are found in the 2. GLS (Fig. 5). Generally, the shape of GR and Si/Al ratio curves are comparable; however, individual sections do not show the same relation between GR and Si/Al ratio.

4.3. Petrography

4.3.1. Grain size and sorting

For well 1, the mean grain size ranges between 0.101 mm and 0.245 mm (very fine to fine sand) and for well 2 from 0.085 mm to 0.233 mm (very fine to fine sand). Whereas no difference is visible between the 1. and 2. GLS for well 1, the 2. GLS in well 2 shows on average finer grain sizes than the 1. and 3. GLS (Fig. 6a). Sorting coefficients after Folk and Ward (1957) for well 1 ranges between 0.78 and 1.53 (moderately sorted to poorly sorted), and no difference between the 1. and 2. GLS is seen. Sorting for well 2 ranges

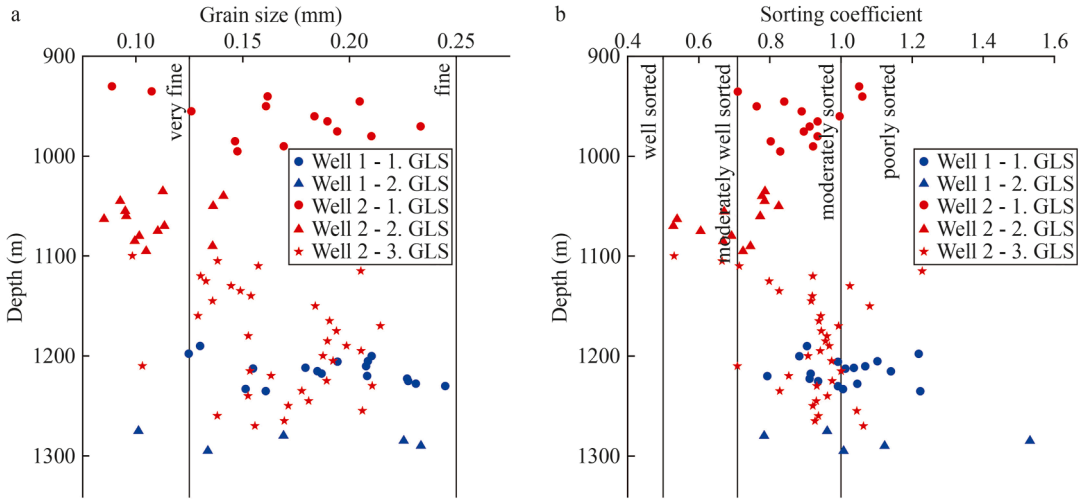

Fig. 6. Grain size and sorting distribution. Cross plot of (a) mean grain size and (b) sorting versus well depth for well 1 (blue) and well 2 (red). The 1. GLS is indicated by circles, the 2. GLS by triangles, and the 3. GLS by stars. (a) Grain sizes for both wells vary between very fine- and fine-grained sand, whereas the top interval between 930 m and 995 m (1. GLS) and the bottom area (1100–1270 m) (3. GLS) comprises on average larger grain sizes than the middle interval (2. GLS) between 1035 m and 1100 m. (b) Sorting for both wells vary between moderately well sorted and poorly sorted. The middle (2. GLS) interval for well 2 shows on average the best sorting (1035–1100 m).

between 0.53 and 1.23 (moderately well sorted to poorly sorted), where the 2. GLS shows on average a slightly better sorting than the 1. and 3. GLS (Fig. 6b). Samples from well 2 also include material from thin intercalated sand bodies in the finer-grained 2. GLS (indicated by higher GR values in Fig. 5d), resulting in generally better sorting and finer grain sizes. Samples from the 2. GLS of well 1 are mostly taken in a coarse-grained section below a finer grained interval (indicated by lower GR in Fig. 5a).

4.3.2. Detrital components

4.3.2.1. Well 1. The main detrital components are quartz grains (47.3 %–80.7 %), K-feldspar (0.3 %–10.0 %), and glauconite (0.3 %–4.3 %) (Fig. 7a). Other detrital components are plagioclase (0–0.3 %), muscovite (0–3.0 %), biotite (0–3.0 %), brownish and greenish chlorite flakes (0.3 %–2.0 %), mudrock fragments (RF) (0–5.3 %), siltstone RF (0–2.7 %), sandstone RF (0–2.3 %), siderite grains (0–1.7 %), calcitic RF and foraminifera (0–1.7 %), ferroan calcitic RF and foraminifera (0–0.3 %), chert (0–3.0 %), phyllite (0–0.7 %), undifferentiated ductile RF (0–0.7 %), metamorphic RF (0–0.7 %), and quartzite (0–0.3 %). Detrital clay minerals are glauconite rims (0–3.3 %), pore-lining illite (0–1.0 %), and pore-filling illite (0–0.7 %). Accessories are rutile (0–0.7 %), zircon (0–1.0 %), tourmaline (0–0.3 %), phosphate grains (0–0.3 %), iron oxide grains (0–0.7 %), and undifferentiated opaque phases (0–0.7 %).

4.3.2.2. Well 2. The most abundant detrital components are quartz grains (37.7 %–73.3 %), K–feldspar (1.3 %–8.0 %), and glauconite (0.7 %–11.7 %) (Fig. 7b). Other detrital components are plagioclase (0–1.7 %), muscovite (0–3.0 %) (Fig. 7c), biotite (0–2.3 %), brownish and greenish chlorite flakes (0–1.3 %), mudrock RF (0–15.7 %), siltstone RF (0–0.7 %), sandstone RF (0–0.7 %), siderite grains (0–3.0 %) (Fig. 7c), calcitic RF and foraminifera (0–3.7 %), ferroan calcitic RF and foraminifera (0–3.3 %) (Fig. 7d), chert (0–2.0 %), phyllite (0–3.0 %), plutonic RF (0–0.7 %), undifferentiated ductile RF (0–1.7 %), metamorphic RF (0–2.3 %), volcanic RF (0–0.3 %), and quartzite (0–2.0 %). Detrital clay minerals are mainly chlorite (0–5.7 %), glauconite rims (0–3.7 %) and pore-lining illite (0–2.7 %), and pore-filling illite (0–1.0 %). Accessories are rutile (0–1.3 %), zircon (0–0.7 %), tourmaline (0–0.3 %), phosphate grains (0–2.0 %), iron oxide grains (0–1.3 %), and undifferentiated opaque phases (0–0.7 %).

4.3.3. Rock composition

The most prominent rock types for well 1 are sublitharenites and subarkose, and subordinately quartzarenites and lithic arkose (Fig. 8). The normalized quartz content varies between 74.3 % and 95.3 %, feldspar between 0.5 % and 13.7 % and rock fragments between 0.4 % and 15.7 %. For well 2 the most prominent rock types are sublitharenites, feldspathic litharenites and subordinately litharenites and subarkose (Fig. 8). The normalized quartz content in well 2 varies between 59.8 % and 86.7 %, feldspar between 2.7 % and 15.1 % and rock fragments between 5.6 % and 30.3 %.

4.3.4. Authigenic phases

4.3.4.1. Well 1. The most abundant authigenic phases are quartz cement (1.7 %–7.0 %), blue-stained pore-filling ferroan calcite cement (0.3 %–18.3 %), and pore-filling siderite cement (0–2.3 %). Furthermore, K-feldspar cement (0.2 %–0.3 %), pore-filling calcite cement (0–2.3 %), purple-stained pore-filling ferroan calcite cement (0–1.3 %), pore-filling dolomite cement (0–1.0 %), pyrite (0–2.0 %), kaolinite cement (0–0.7 %), and Fe-oxide cement (0–0.3 %) occur. Also, partially pore-filling cements as ferroan calcite (0–0.3 %), and dolomite (0–0.3 %) are present. Vein cements are grouped into calcite veins (0–0.3 %), ferroan calcite veins (0–4.7 %) and intragranular ferroan calcite veins (0–1.3 %). Replacive phases are subdivided into kaolinite replacing muscovite (0–0.3 %), kaolinite replacing K-feldspar (0–2.0 %), illite replacing kaolinite (0–0.7 %), illite replacing K-feldspar (0–1.0 %) and Fe-calcite replacing K-feldspar (0–1.3 %).

4.3.4.2. Well 2. Quartz cement is the main authigenic phase (1.3 %–11.7 %), followed by blue-stained pore-filling ferroan calcite cement (0.3 %–24.7 %), and pore-filling siderite cement (0–4.3 %). Furthermore, K-feldspar cement (0–1.3 %), pore-filling calcite cement (0–0.3 %), purple-stained pore-filling ferroan calcite cement (0–1.7 %), pore-filling dolomite cement (0–1.3 %), pyrite (0–1.0 %), kaolinite cement (0–1.0 %), and Fe-oxide cement (0–1.0 %) occur. Also, partially pore-filling cements as purple- and blue-stained ferroan calcite (0–0.7 %), partially pore-filling siderite cements (0–1.7 %) and dolomite (0–0.3 %) are present. Vein cements are calcite veins (0–0.3 %), ferroan calcite veins (0–3.3 %) and intragranular ferroan calcite veins (0–0.7 %). Replacive phases

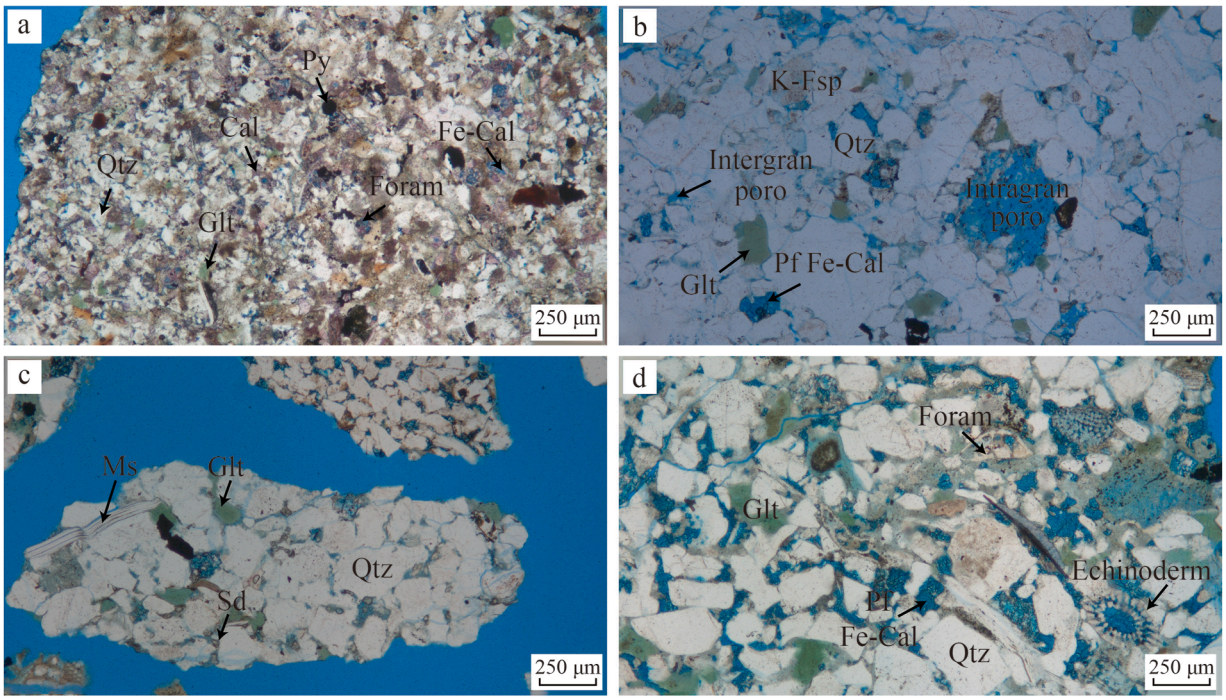

Fig. 7. Thin section microphotographs of individual cuttings from well 1 and well 2 from different depths. (a) Well 1 (depth 1190 m), individual sandstone cuttings show smaller grain sizes and are composed of e.g., detrital quartz (Qtz), foraminifera (foram) with calcitic tests (Cal), glauconite (Glt), and inter- and intragranular ferroan calcite cements (Fe-Cal). (b) Well 2 (depth 940 m), intragranular porosity (intragran poro) in former feldspar and intergranular (intergran poro) porosity is visible as optical porosity. Besides detrital quartz, glauconite and feldspar occur, as well as pore-filling (pf) Fe-Cal. (c) Well 2 (depth 1150 m), siderite (Sd), quartz grains, glauconite occurs as well as muscovite (Ms). (d) Well 2 (depth 1045 m), some individual cuttings are rich in bioclasts, e.g., foraminifera and echinoderm fragments. Ferroan calcite cements (Fe-Cal) fills former pores in bioclasts (e.g., echinoderm fragments).

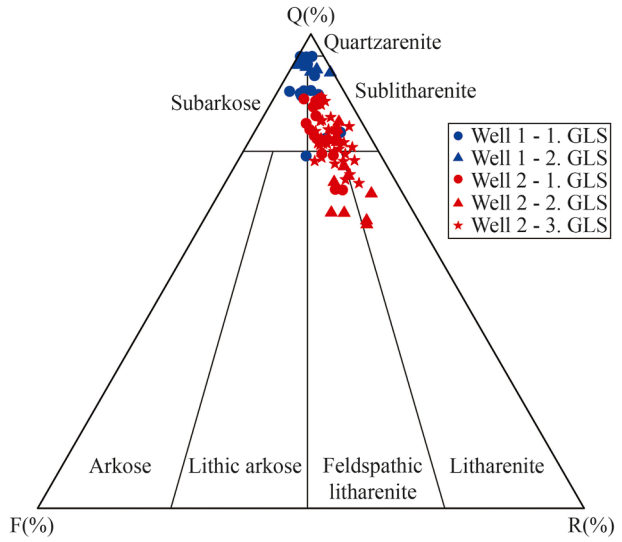

Fig. 8. Ternary classification for sandstones (Q = quartz, F = feldspar, R = rock fragments) according to Folk (1980) for well 1 (blue) and well 2 (red). Sandstone cuttings are in general quartz rich, showing rock compositions of sublitharenites, subarkose, and subordinate quartzarenites and lithic arkose for well 1, and sublitharenites, feldspathic litharenites and subordinate litharenites and subarkose for well 2.

occur as kaolinite replacing muscovite (0–0.7 %), kaolinite replacing K-feldspar (0–0.7 %), illite replacing kaolinite (0–0.3 %), illite replacing K-feldspar (0–1.0 %) and Fe-calcite replacing K-feldspar (0–2.0 %).

4.3.5. Optical porosity

4.3.5.1. Well 1. Optical porosity is mainly represented by intergranular porosity (0.3 %–1.7 %) and intragranular porosity (0–1.7 %) mainly after K-feldspar dissolution. Additionally, intragranular porosity in undifferentiated RF (0–0.3 %), and fracture porosity (0–2.3 %) occur.

4.3.5.2. Well 2. Intergranular porosity (0–2.3 %) is the main type of optical porosity (Fig. 11d), followed by intragranular porosity in K-feldspar (0–2.3 %) (Fig. 11g). Additionally, intragranular porosity in carbonate grains (0–0.3 %), and in undifferentiated RF (0–1.0 %) occurs.

4.4. Intergranular volume (IGV)

The *IGV* for well 1 range from 7.7 % to 25.7 %, and for well 2 from 9.0 % to 31.7 %. The *IGV* shows no correlation to the GLS formation or depth (Fig. 9a), and low correlations with detrital quartz and feldspar contents (Fig. 9b) for wells 1 and 2, showing lower *IGV* at higher detrital quartz and feldspar contents. A general correlation with sorting (Fig. 9c) with well to moderately well sorted samples showing higher median *IGV* than poorly sorted samples (Fig. 9c). Furthermore, a slightly negative correlation between *IGV* and grain size can be seen in samples from well 2 (Fig. 9d). While only two samples from well 1 fall in the very fine sand category, the overall decrease in *IGV* with increasing grain size, based on the median values can still be matched between both wells. The main pore-filling cement types (quartz and carbonates) show different correlations to the *IGV*. The impact of quartz cement on *IGV* is only minor (Fig. 9e), and more pronounced for pore-filling and partially pore-filling carbonate cements (Fig. 9f), especially for well 1 ($R^2 = 0.93$).

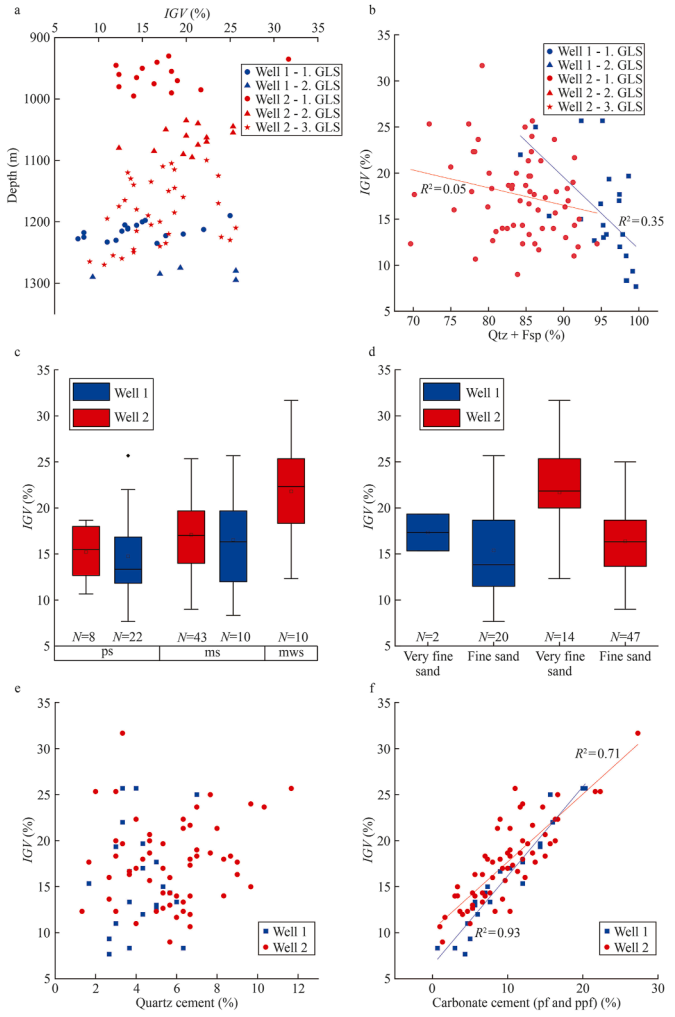

Fig. 9. *IGV* cross plots with depth, detrital quartz + feldspar content, sorting, grain size classes, quartz cement and carbonate cements. (a) *IGV* shows no correlation with well depth, nor with the 1., 2. or 3. GLS. (b) *IGV* shows low correlation with detrital quartz and feldspar content for wells 1 and 2. (c) Overall, better sorting is correlated to higher *IGV*, whereas moderately well sorted samples from well 2 show highest *IGV*, ps: poorly sorted, ms: moderately sorted, mws: moderately well sorted. (d) Very fine sand grain size class in well 2 shows higher *IGV* values compared to fine sand. (e) *IGV* shows no correlation with quartz cement. (f) *IGV* versus pore-filling (pf) and partially pore-filling (ppf) carbonate cements with a very high positive correlation for well 1 and a high correlation for well 2.

4.5. Correlation of grain size, sorting, and glauconite content

Grain size and sorting show a positive correlation for well 2, but not for well 1 (Fig. 10a). The glauconite content varies with well depth and shows a positive correlation for well 2, but no correlation for well 1 (Fig. 10b). However, the glauconite content in well 2 is especially elevated in the 3. GLS (stars in Fig. 10b), which was not sampled in well 1. The glauconite content in the 1. and 2. GLS of wells 1 and 2 is comparable.

4.6. Paragenetic relationships

As the paragenesis and mineralogical composition of individual cuttings in the two observed wells show no large difference, the paragenetic relationships are described together for the studied sections of the GLS in the Vienna Basin Flysch play.

Quartz grains display syntaxial quartz overgrowth cements. Glauconite or chlorite rims which are occasionally present outline grains such as quartz or occur between quartz grains and their syntaxial overgrowths (Fig. 11a and b). Beside chlorite and glauconite, pore-lining tangential illite is rarely encasing detrital grains such as quartz. Quartz grains and their syntaxial quartz overgrowths are encased by pore-filling Fe-Cal (stained blue, Fig. 11a) if present, which also fills former pores in bioclasts (Fig. 7d). The Fe-Cal can also occur partially pore-filling in individual cuttings. Besides the blue-stained (partially) pore-filling Fe-Cal, purple-stained Fe-Cal or calcite (red staining, Fig. 7a) pore-filling cements show the same paragenetic relationships as Fe-Cal. The partially pore-filling siderite is present as brownish elongated rhombs with a high relief (Fig. 7c and 11e), either embedded in chloritic matrix or outlining detrital grains, and occasionally encased in quartz cement. Chlorite and glauconite also fill chambers of foraminifera with calcitic tests. Pyrite occurs as framboidal or cubic aggregates in some cuttings (Fig. 7a), in rock fragments or filling individual foraminifera tests and is most prominent in samples rich in limestone rock fragments (Fig. 11c). Furthermore, pyrite occurs at the host rock-vein interface in one sample (Fig. 11j). Intergranular Fe-oxide cements occur only rarely, showing a red color at the rim of opaque grains.

In some individual cuttings feldspar grains, feldspar cement and/or intragranular feldspar dissolution can also be observed, the latter resulting in intragranular porosity (Fig. 7b). In some samples the intragranular dissolution pores from K-feldspar (K-Fsp) grains are filled by replacive Fe-Cal cement (Fig. 11f), but these uncompacted intragranular pores can locally be filled with kaolinite, showing a vermicular structure (Fig. 11g). However, individual open intragranular pores are also noted within K-Fsp and undifferentiated RF. Besides the replacement of K-Fsp, kaolinite replaces muscovite in individual cuttings, and can also occur as cement filling intergranular pores. Illite replaces individual kaolinite particles or K-Fsp grains.

Based on optical evaluations, different fracture and vein generations are identified. In general, the veins are of calcitic or Fe-calcitic composition and can also occur as trans- or intragranular veins (Fig. 11c). Some of the Fe-calcitic veins are not only stained blue, but also purple. Additionally, blue-stained partially sealed veins occur (Fig. 11i). The veins will be further evaluated in the next section.

Cataclastic shear bands composed of small, angular, and densely packed quartz grain fragments, preserving little to no optical porosity (Fig. 12a and b), are found only rarely within individual cutting fragments of both wells, and some of them are crosscut by carbonate veins (Fig. 12c). The shear bands do not show intergranular carbonate cement and are devoid of deformed glauconite grains (Fig. 12a and b).

In contrary, artificial cataclastic fragments show high optical porosity and parallel fracturing within grains in all studied cutting samples (Fig. 12d). They are prominently visible as white cutting fragments (S-C clast in Fig. 3b). Here, the cataclastic zone contains ground-up intergranular ferroan calcitic cements and deformed glauconite grains.

4.7. Cold cathodoluminescence

Cathodoluminescence (CL) on polished thin sections show different brightness of luminescence for Fe-Cal cements and Fe-Cal vein generations (Figs. 13 and 14). Furthermore, the luminescence of detrital K-Fsp grains is bright blue, detrital quartz grains show a mostly dark blue luminescence, whereas quartz overgrowth cements are non-luminescent (Fig. 13a–d). Siderite shows no luminescence, whereas the interstices are filled with orange luminescent Fe-Cal. Pervasively sealed veins generally show a

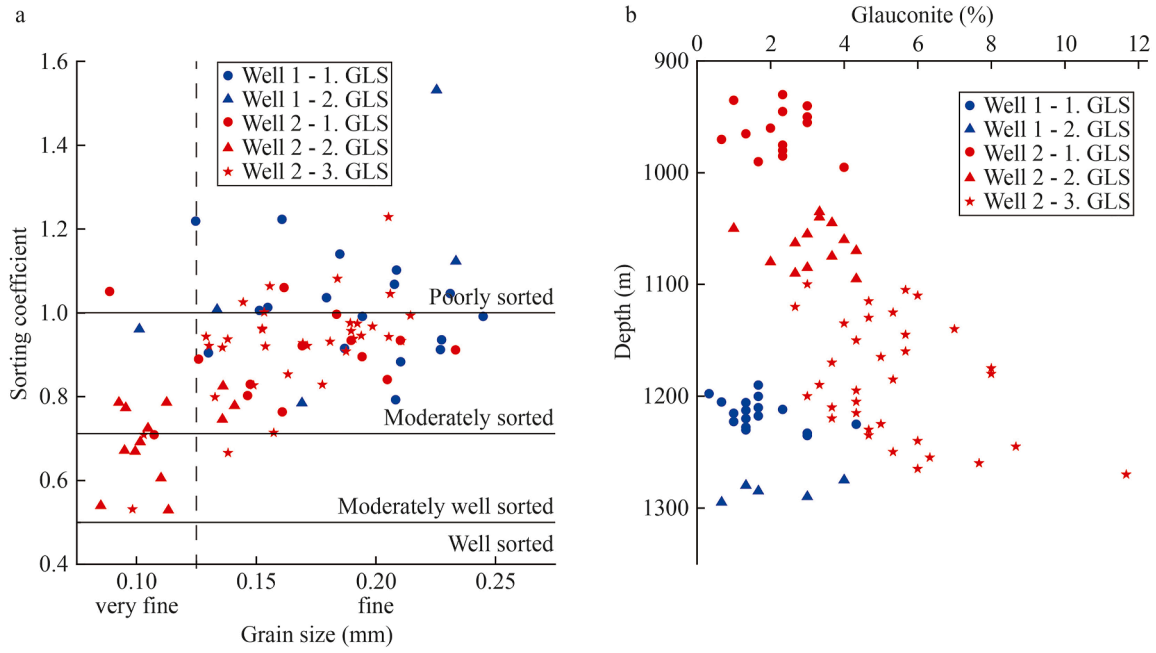

Fig. 10. Sorting vs. grain size and glauconite content vs. depth cross plots. (a) Sorting after Folk and Ward (1957) and grain size after Wentworth (1922) in Folk (1980) show a positive correlation for well 2 (red), whereas well 1 (blue) shows no correlation. The different GLS intervals are given in circles (1. GLS), triangles (2. GLS) and stars (3. GLS). (b) The glauconite content obtained from point counting shows elevated glauconite contents in the 3. GLS as opposed to the 1. and 2. GLS in well 2.

slightly brighter orange luminescence, whereas the pore-filling cement shows a darker luminescence (Fig. 13a), although the differences may be minute (Fig. 14). Based on the cross-cutting relationships of the pervasively sealed veins, three generations can be differentiated. The first generation shows a dull luminescence, and is crosscut by the two following generations (Fig. 13a and b). The two other generations show a bright and dull luminescence, respectively. The bright luminescing phase is crosscut by the dull luminescing phase in other cutting samples (Fig. 14b).

Partially sealed veins show an orange luminescence at the center of rhombic crystals composed of Fe-Cal and a dull rim of Fe-Dol (Fig. 13b and c). Intercrystalline porosity is preserved within partially sealed carbonate veins containing euhedral rhombs (Fig. 13c). Additionally, some cuttings show formerly fractured quartz grains, which are healed by quartz cement, showing no luminescence (Fig. 13d).

4.8. Bulk drill cutting pXRF comparison to petrography

Iron and magnesium contents obtained from bulk drill cuttings pXRF may suggest a generally positive relation with the sum of the mostly ferroan calcitic carbonate cements including veins (Fig. 15a) and with minerals containing iron (glauconite, Fe-calcite, siderite, pyrite, opaques, Fe-oxides, mudrock RF, biotite, and chlorite) (Fig. 15b) obtained from point counting. While R^2 values are moderate to low (R^2 from 0.2 to 0.4) for the correlation of Fe + Mg contents with both mineral contents, median values of Fe + Mg contents increase with increase in carbonate cement (incl. veins) and Fe-bearing mineral contents.

4.9. Correlation to production data

To find potential proxies for production intervals from drill cuttings, several properties and results were compared with known producing and non-producing intervals for both wells. Based on the overlap of interquartile ranges (IQR, P25 to P75), we decide between distinctly different and indifferent properties. Therefore, the IQRs of either producing and non-producing intervals should not overlap with each other for more than 25 % (50 % of the IQR). Producing intervals show lower Fe + Mg ratios, lower optical porosity, and contain more total vein cements (Fig. 16b–e, f). The Si/Al content observed from pXRF, the Ca/Mn, and total carbonate cement content including veins for producing and non-producing intervals are largely overlapping and may therefore not be good criteria to assess the producibility of prospective intervals (Fig. 16a, c, d).

5. Discussion

5.1. GR and pXRF

The 1. to 3. GLS are composed of roughly 70 % of massive sandstone beds of proximal turbidites (Rammel, 1989). The comparison between the geochemical fingerprint i.e., lower Si/Al ratio, obtained from pXRF measurements, fits well with higher GR data in areas of higher clay content (Fig. 5). Generally, higher Si/Al ratios (>8) and low GR values are indicative for sandstone (e.g., Rider and Kennedy, 2011; Craigie, 2018). However, the mineralogical composition of the studied sandstones contains K-bearing minerals as feldspar or mica, K-bearing phyllosilicates such as glauconite and illite, and mudrock RF. This may enhance the amount of potassium, thorium and uranium, leading to overall higher GR signals, even in sandstone-rich sections (e.g., Rider, 1990; Johan and Neil, 2001; Rider and Kennedy, 2011).

A minor shift between the depth ranges of peaks in Si/Al and GR plots is observable in some intervals (Fig. 5), which might result from averaging GR data over 5 m intervals to match the sample depth ranges. As the provided bulk cutting samples also contain mudrock fragments, it is not excluded that the mudrock content is underrepresented within the samples as mudrocks are more easily ground up especially along the planar lamination of the mudrocks. This may influence the pXRF measurements, but the impact is

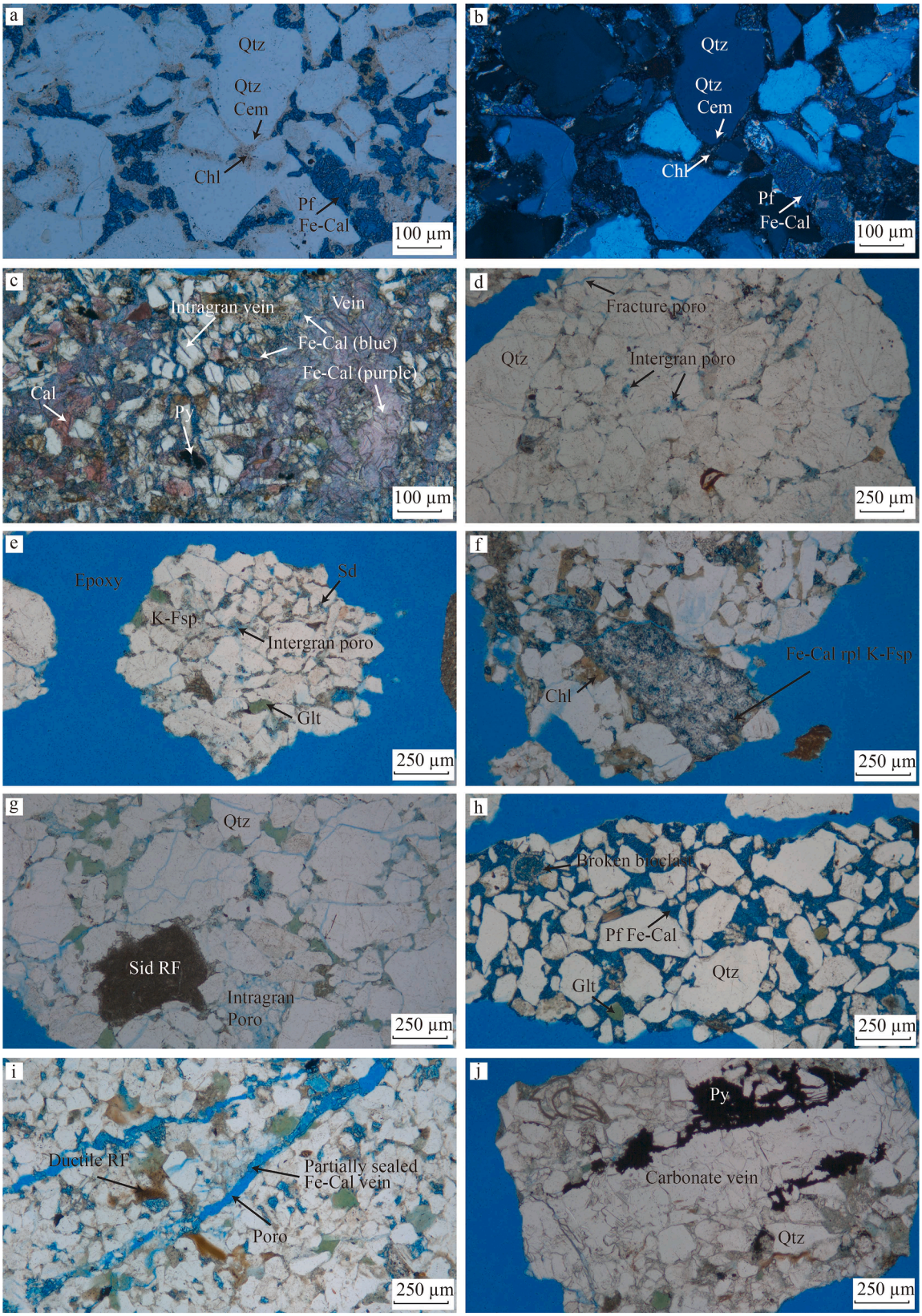

Fig. 11. Photomicrographs showing mineralogical and structural elements. (a) Quartz grains (Qtz) and quartz cement (Qtz cem) with grain lining chlorite (Chl), and crossed-polarized in (b) (well 2, depth 950 m). (c) Well 1 (depth 1190 m), individual cuttings, containing calcite grains (Cal, stained red) are cemented by pore-filling ferroan calcite (Fe-Cal, stained blue). Veins are either composed of blue Fe-Cal or purple Fe-Cal. The veins outlining or penetrating grains as well as forming intragranular veins (intragran vein) in detrital grains such as quartz. (d) Individual cuttings show carbonate veins with pyrite (Py) at the transition to the host rock (well 2, depth 955 m). (e) Siderite (Sd) occurs as single crystals filling intergranular pores (well 1, depth 1233 m). (f) Detrital quartz is enclosed by brownish chlorite, which is encased by pore-filling Fe-Cal (blue) and also replaces K-feldspar (K-Fsp) (well 2, depth 1140 m). (g) Detrital siderite grain (Sid RF). The dissolution of K-Fsp leads to the formation of intragranular porosity (intragran poro) (well 2, depth

interpreted as minor, as the Si/Al ratio is comparable to borehole GR data (Fig. 5). For an individual section from 1160 m to 1210 m, a higher Ca content is measured and is related to higher contents of carbonate rock fragments and bioclasts observed in microscopic analyses. As log trends can be used to assess stratigraphic properties (Milton and Emery, 1996), their comparison to Si/Al trends may thus enable the cross check if the derived cutting depth interval may be linked to log depth and evaluate the representativeness of cutting composition (i.e. relative proportions of sandstone and mudrock cuttings).

Natural fractures play an important role for reservoir exploration, production and well planning, as they may be the main fluid conduit in tight sandstone reservoirs and many carbonate reservoirs (e.g., Olson et al., 2009; Bahrami et al., 2012; Lamarche et al., 2012; Khelifa et al., 2014; Becker et al., 2018). Care has to be taken when assessing fractures as open, uncemented fractures are not preserved in cuttings. Thus, their intensity (i.e. number of fractures per meter) and aperture cannot be reconstructed from cuttings, but could be deduced from borehole image logs (e.g., resistivity or acoustic image logs) (e.g., Fernández-Ibáñez et al., 2018) or core material. However, partially sealed veins and their composition may not be visible in image logs due to, e.g., uncertainties of log interpretation (Fernández-Ibáñez et al., 2018) and the resolution of the measurements. Consequently, cuttings and petrographic analyses are a way to show if a fracture is partially sealed and with which mineral. The assessment of the amount and locations of partially sealed fractures affects the reservoir development e.g., during acidizing in carbonate-bearing lithologies (Knox and Ripley, 1979). However, depending on the well direction, only certain fracture orientations are observed (Terzaghi, 1965). In the absence of orientated core material, the occurrence of veins and partially sealed veins can be identified from cuttings, by using a binocular microscope (Fig. 3) (e.g., Tiainen et al., 2002). Cuttings may therefore still preserve information on vein paragenesis to further constrain the amount and temporal succession of several natural fracturing events.

The pXRF-based Fe + Mg measurements were conducted on bulk drill cutting from respective sample depths, composed of different sandstone and mudrock lithotypes. Carbonate cement in pores and veins is reflected by mostly ferroan calcite, dolomite and siderite in sandstone cuttings. With increasing carbonate cement contents (incl. veins) a general increase in median Fe + Mg contents can be observed (Fig. 15a). As carbonate cements are the main pore-filling and vein cement phases, this correlation may be used as a first pass RQ assessment if producing intervals are related to elevated vein cement contents (Fig. 16f).

5.2. Mineralogy and texture

The two studied wells show a similar mineralogic composition using petrographic tools such as point counting, whereas the quartz-content varies slightly within the wells (higher in well 1, Fig. 8) and GLS but is largely comparable for the 1. GLS in both wells (avg. 1. GLS well 1: 67.8 %, avg. 1. GLS well 2: 59.6 %). However, well 1 also shows higher amount of Si measured with pXRF (Fig. 4a), which can explain the higher quartz content of well 1 samples in the QFR plot (Fig. 8). The overall rock types (sublitharenites, subarkose, quartzarenites, and lithic arkose for well 1; sublitharenites, feldspathic litharenites, litharenites, and subarkoses for well 2) are in accordance to rock descriptions by Rammel (1989), analyzing the equivalent sediments from the Wienerwald Flysch, where the sandstones are described as mostly quartzarenites, and also sublitharenites and subarkose. Likewise the observed moderate to poor sorting of the cutting samples (Fig. 6) is comparable to the core study by Rammel (1989). The distance between the two observed wells is less than 1 km and both samples are covering the same formations (1. to 3. GLS) of a turbidite sequence which is known to be regionally present. This explains the observed similarities of the petrographic results from both wells.

The 3. GLS shows higher glauconite contents than the overlying 1. and 2. GLS. As only well 2 covers all three GLS sections (Fig. 10b), this could not be verified in well 1. The average glauconite content for well 1 (1.8 %) is lower as described in Sauer et al. (1992) but average glauconite content in well 2 (4.2 %) is in general in accordance, as the glauconite content in the Glauconite Sandstone Fm. is given between 5 % and 10 %. While generally the glauconite content in sediments increases in transgressive stages at climate optima (Amorosi, 2013; Santanu et al., 2016; Baioumy et al., 2020; Tribovillard et al., 2023), the studied sedimentary rocks of the GLS represent turbidite deposits (Rammel, 1989). Therefore, we interpret the glauconite as redeposited. Nevertheless, the turbidite deposits may still record the changes affecting the "glauconite factory" (sensu Tribovillard et al., 2023) in shallower water depths, prior to redeposition. Although absolute age data for the studied lithologies are not available, the recorded change in glauconite content may be linked to the "Paleocene/Eocene Thermal Maximum, Middle Eocene Climatic Optimum" and subsequent climatic deterioration and cooling (Sotak, 2010) known to have affected the nearby Pannonian and Carpathian Basins. Higher glauconite contents in the 3. GLS are therefore interpreted to result from higher glauconite production in shallow water depth at higher surface temperatures, whereas a lower glauconite production during the deposition of the 1. and 2. GLS is interpreted to be linked to subsequent climatic cooling (Sotak, 2010).

Individual samples are affected by different grade of carbonate cementation (e.g., pore filling and partially pore filling carbonate cements in well 1: 0.7 %–20.3 %, and well 2: 1.0 %–30.7 %). Within the samples, individual cuttings show fully cemented pores by e.g., Fe-Cal (Fig. 11h), whereas in others the pores and veins are only partially cemented. Additionally, locally found loose quartz grains within the samples indicate less intensely cemented sections, which were then very likely disaggregated during the drilling process. This is in contrast to Sauer et al. (1992) where quartz cement and glauconitic clay minerals are mentioned as main permeability reducers.

5.3. Compaction and porosity

The *IGV* shows no correlation with depth or the GLS subdivision (Fig. 9a), and also low correlation with the detrital quartz and feldspar content for wells 1 and 2 (Fig. 9b). For well 1, the *IGV* is lower for samples containing higher detrital quartz and feldspar grain contents, while typically the *IGV* should be higher with increasing detrital quartz and feldspar contents as they act as rigid grains, where mechanical compaction is less severe than in rocks with higher contents of ductile components (Rossi and Alaminos, 2014). Well to moderately well sorted samples show in general higher median *IGV* than only poorly sorted samples (Fig. 9c). Additionally, the *IGV* show slight negative correlation with grain

1140 m). (h) Sandstone cutting with detrital quartz grains, pore-filling ferroan calcite cements, glauconite and broken bioclasts (well 1, depth 1250 m). (i) Completely cemented and partially sealed veins with Fe-Cal in cutting fragment containing ductile RF (well 2, depth 1060 m). (j) Individual cuttings contain carbonate veins with pyrite at the transition to the host rock (well 2, depth 955 m).

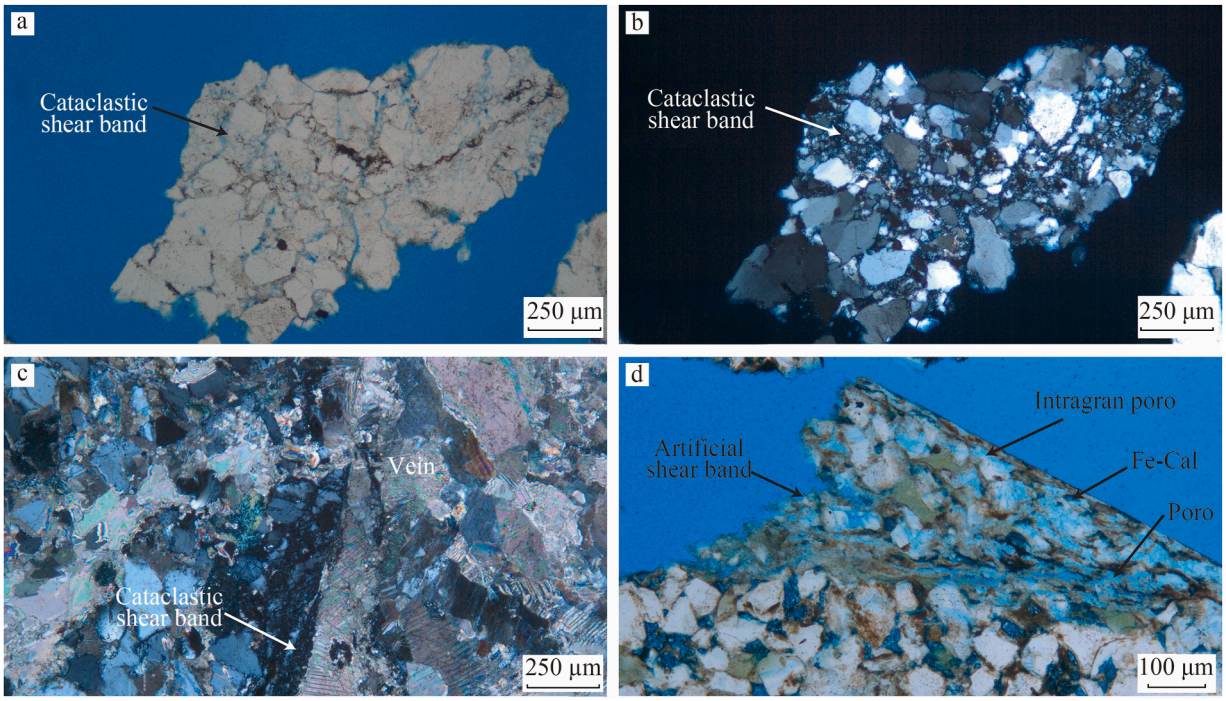

Fig. 12. Cataclastic shear bands in individual cuttings. Natural cataclastic shear band (a), grain rearrangement and angular small grain sizes are more visible under crossed polarizers (b) (well 1, depth 1197.5 m). (c) An individual cutting contains a natural cataclastic shear band with angular, densely packed small grains. The shear band is cross cut by a carbonate vein (xpl, well 1, depth 1212.5 m). (d) Artificial shear bands are mostly seen at cutting boundaries, and missing parts of grains (now intragranular porosity, intragran poro), contain ground up Fe-Cal cements, and unsealed, fractured grains around the shear band (well 2, depth 1135 m).

size in well 2 (Fig. 9d), thus, samples with smaller grain sizes show higher *IGV* (Fig. 9d). Theoretically, finer grained and more poorly sorted samples should be characterized by a lower *IGV* (Beard and Weyl, 1973). Therefore, the observed correlation indicates that finer grained sediments have generally higher *IGV*, due to higher carbonate cement contents, as pore-filling and partially pore-filling carbonates show a positive correlation with *IGV* (Fig. 9f, well 1 $R^2 = 0.93$, well 2 $R^2 = 0.71$). Furthermore, the lower degree of compaction in finer grained samples may be due to detrital clay mineral matrix contents.

Low optical porosity is therefore due to both cementation and detrital clay mineral matrix contents (in very fine sand sized samples) and compaction (in fine sand sized samples), as seen in deformation of ductile RF and undifferentiated RF (Fig. 11i). However, investigating samples with increasing depth would be difficult to establish on core data as cores are never continuous taken. Our investigation can therefore be used to confirm and refine the (indirect) log interpretation.

5.4. Paragenetic sequence

For this study the diagenetic sequence is subdivided into early and burial diagenesis. Furthermore, indicators for telogenesis and thus interaction with meteoric water following burial diagenetic conditions are missing. Though the studied succession is subdivided into three sections (1.–3. GLS) the units in the two observed wells show similar mineralogical characteristics. Therefore, one summarizing paragenetic sequence is presented (Fig. 17).

5.4.1. Early diagenesis

As chlorite and pore-lining illite rim individual grains or are present between grains such as e.g., quartz and their syntaxial overgrowth cement (Fig. 11a), a depositional origin before compaction and cement formation is interpreted. This is in agreement with depositional models for turbidite/flysch deposits (Cummins, 1962). Glauconite occurs as individual grains (e.g., Fig. 7b) or as rims outlining grains in individual cuttings. Glauconite is described as the earliest stage in the paragenesis, as the differentiation between authigenic and detrital glauconite is not possible since the flysch consists of turbidite layers (Rammel, 1989).

Siderite rhombs are observed embedded in chlorite matrix, outlining detrital grains and encased in quartz cement. Therefore, an early diagenetic origin is interpreted. This is in agreement with interpretations from other marine and deltaic sections which are also occasionally found to be glauconite bearing (Morad et al., 2002; Adamolekun et al., 2022; Greve et al., 2024). Siderite most likely formed in iron reduction zones (Morad, 1998).

Pyrite observed as cubic crystals in intergranular pores, framboids and pore-filling in bioclasts such as foraminifera most likely originate from bacterial sulphate reduction (BSR) processes in shallow burial environments (Berner, 1970; Coleman, 1985; Morad, 1998). Therefore, the pore water needs to be anoxic and a certain amount of dissolved sulphate must be available (Morad, 1998). The BSR leads to an increase in alkalinity, which may enhance the precipitation of carbonate cements (Berner, 1970; Morad, 1998).

5.4.2. Burial diagenesis

Mechanical compaction, grain rearrangement and deformation of ductile components such as ductile rock fragments or phyllosilicates, squeezed into pore spaces, reduces porosity and *IGV*. Compaction is interpreted to initiate during early diagenesis, following the emplacement of the chloritic and illitic matrix, as both minerals are prominently found in between detrital grains (e.g., Busch et al., 2024).

Quartz cements partially encase chlorite and siderite, and all three phases are encased in Fe-Cal. Thus, the formation of Fe-Cal

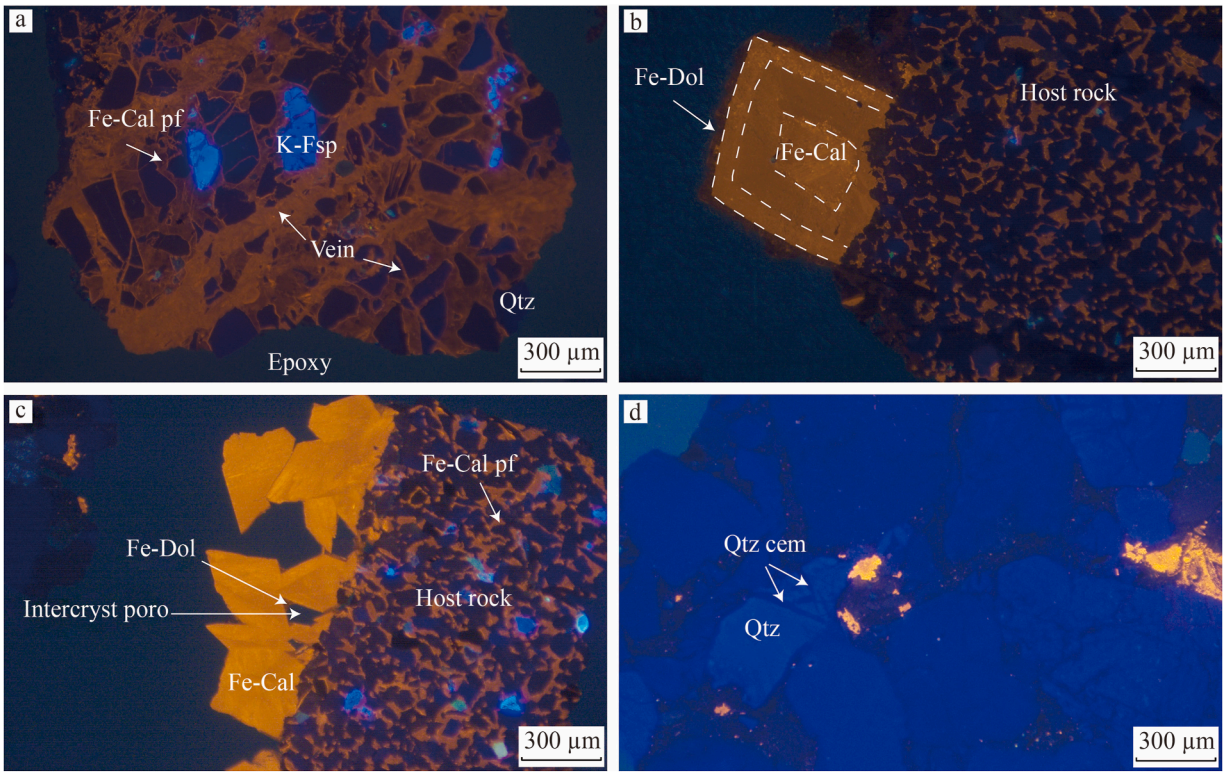

Fig. 13. Photomicrographs of cold cathodoluminescence showing luminescence properties of detrital and authigenic minerals, and veins for individual drill cuttings from well 1 and well 2. (a) Pore-filling (pf) Fe-Cal shows dull luminescence, whereas the veins, penetrating the host rock and individual grains, show a brighter luminescence. Quartz shows a dark blue luminescence and K-feldspar (K-Fsp) bright blue (well 2, depth 935 m). (b) Euhedral shaped carbonate crystal with zonation, showing a bright center, followed by a less bright zone, and a dull Fe-Dol rim. The host rock cement luminescence is less bright than the vein. The euhedral crystal shape and absence of pervasive cements indicates a partially sealed vein (well 2, depth 1035 m). (c) The partially sealed vein with euhedral crystal facets shows a brighter luminescence than the pore-filling cement in the host rock. Also, the euhedral shape preserves intercrystalline porosity (intercryst poro), and they are encased by a dull Fe-Dol phase (well 2, depth 1090 m). (d) Fractured and cemented quartz grains showing no luminescence quartz cement (well 1, depth 1215. m).

postdates chlorite emplacement, siderite, and quartz cement formation. Generally, quartz precipitation rates are elevated at temperatures above 70 °C (Walderhaug, 2000; Lander et al., 2008) and is related to burial diagenesis (Morad et al., 2002). Authigenic quartz cements including fracture healing cements in quartz grains (Fig. 13d) show dark and non-luminescent areas in CL around or inside detrital quartz as described by Demars et al. (1996). The blue luminescing detrital quartz grains may be indicative of an igneous origin or fast cooled high-grade metamorphic rocks (Götze et al., 2001 and references therein). The healed intragranular fractures in quartz grains (Fig. 13d) may indicate grain fracturing during mechanical compaction (Wilson et al., 1994), pre-dating quartz cementation. As chemical compaction with convex-concave and sutured contacts is rarely observed, the main source for quartz cement is interpreted to be from K-Fsp dissolution and clay mineral recrystallization (e.g., Worden and Morad, 2003).

Partially dissolved K-Fsp grains still retain their grain shape, therefore, dissolution of K-Fsp is interpreted as a burial diagenetic process ensuing after compaction, rarely followed by the formation of kaolinite (e.g., Morad et al., 2010). Feldspar dissolution is most likely the result of interaction with acidic formation waters (Worden and Morad, 2003), which is supported by the preservation of kaolinite, the latter is stable at low K^+/H^+ ratios (Lanson et al., 2002). The analyzed samples show a sandstone-mudrock alternation, organic acidic fluid may originate from maturation of organic matter in mudrock layers or associated to source rock maturation (Lanson et al., 2002 and references therein). Thus, kaolinite can form due to acidic fluids and the reaction with feldspar. The distribution of illite/kaolinite or the replacement of kaolinite by illite depends on the availability of potassium. Potassium may be derived from influx of potassium-rich waters or dissolution of potassium-bearing minerals e.g., K-Fsp and temperature (Lanson et al., 2002). Therefore, a low potassium-content and low temperatures inhibit the alteration of kaolinite to illite, as well as low K^+/H^+ ratios, which favors kaolinite formation (Lanson et al., 2002). The formation of illite from kaolinite is often shown in relatively deeply buried sandstones as opposed to precipitation from a kaolinite precursor in relatively shallowly buried sandstones, e.g., on the Norwegian Continental Shelf (Lanson et al., 2002 and references therein). Furthermore, kaolinite replacing mica was observed in individual cuttings. Kaolinite replacing mica is one of the dominant types of diagenetic kaolinite in sandstones (Lanson et al., 2002 and references therein). The other dominant types are vermiform and blocky kaolin, whereas their crystallization conditions are controversial (Lanson et al., 2002). One of the hypotheses is the formation of vermiform and blocky kaolin at shallow burial depth by interaction with fluids of meteoric origin during early diagenesis or after inversion. The other hypothesis is that the mixture of meteoric fluids and organic acid-rich or CO_2-rich fluids might be responsible for feldspar alteration and kaolinite precipitation, with the altering fluids resulting from maturation of organic matter, e.g., from mudrocks (Lanson et al., 2002 and references therein). As the kaolinite booklets are preserved in uncompacted intragranular pores, the latter formation pathway is interpreted for the studied samples.

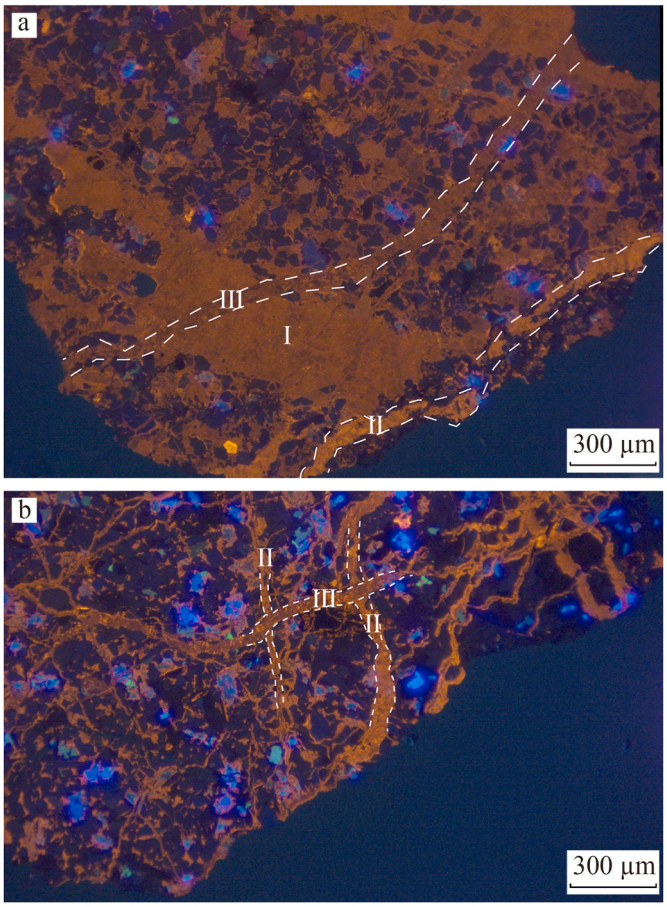

Fig. 14. CL photomicrograph highlighting vein generations. CL photomicrograph showing three generations of sealed veins crosscutting each other of an individual cutting (well 1, depth 1212 m). (a) The different generations (I, II, III) are distinguished using the CL luminescence color, indicating a slightly change of Mn and Fe-contents. (b) Crosscutting relation of vein generation II and III.

Illite is rarely observed to replace K-Fsp and kaolinite, and occurrence of both is possible due to slow reaction rates at lower temperatures (Worden and Morad, 2003 and references therein). Given that illite authigenesis is generally related to temperature (Morad et al., 2002) and common at temperatures >70 °C, a burial diagenetic formation is supported. However, as individual feldspar grains show replacement by Fe-Cal (Fig. 11f) but other K-Fsp grains preserve intragranular pores, two phases of K-Fsp dissolution and alteration before and after carbonate cementation are interpreted. As kaolinite and illite replacements are not observed encased in carbonate cement, their formation is interpreted to postdate Fe-Cal cement precipitation. The occurrence of dissolved feldspar and the formation of secondary porosity or replacement by kaolinite or carbonate cement is comparable to the description by Gier et al. (2008) for Miocene sandstones from the Vienna Basin.

The ferroan calcite cements (Fe-Cal) encase quartz cement overgrowths, partially pore-filling siderite, and fill residual porosity remaining in clay mineral matrix-rich sandstone cutting samples, thus the formation of Fe-Cal is interpreted to post-date the formation of all other diagenetic products. The formation of Fe-Cal cements in sandstones can be caused by elemental uptake from claystones as described by Miocic et al. (2020), which would match the interstratified depositional sequence of flysch deposits. A direct relation to marine carbonate cementation is unlikely as Fe-calcite cement postdates most burial diagenetic phases. Similarly, in a different study of Neogene sandstones from the Aderklaa-78 well in the Vienna Basin, the Fe-Cal cement is the most important porosity reducer (Gier et al., 2008). However, the Fe-Cal cements from the Aderklaa-78 well are interpreted to originate from dissolved detrital limestone rock fragments (Gier et al., 2008). In the studied samples, the detrital carbonate rock fragments are still intact (Fig. 11c), therefore we do not imply a similar source.

5.4.3. *Structural diagenesis*

Natural shear bands, such as deformation bands, are localized deformation structures and characterized by their microstructure

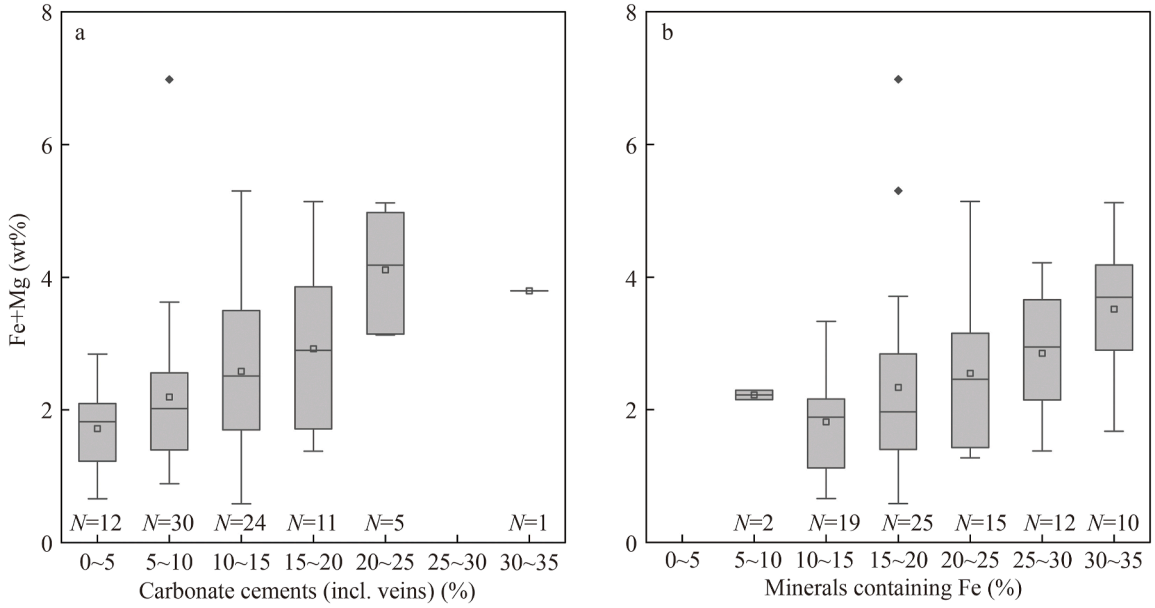

Fig. 15. Box-and-whisker bars plotted for bulk drill cuttings pXRF and petrographic point-counting results, combined for both wells. Iron (Fe) plus magnesium (Mg) content (wt%) is in general higher in samples with higher amount of (a) carbonate cements (incl. veins) and (b) minerals containing Fe.

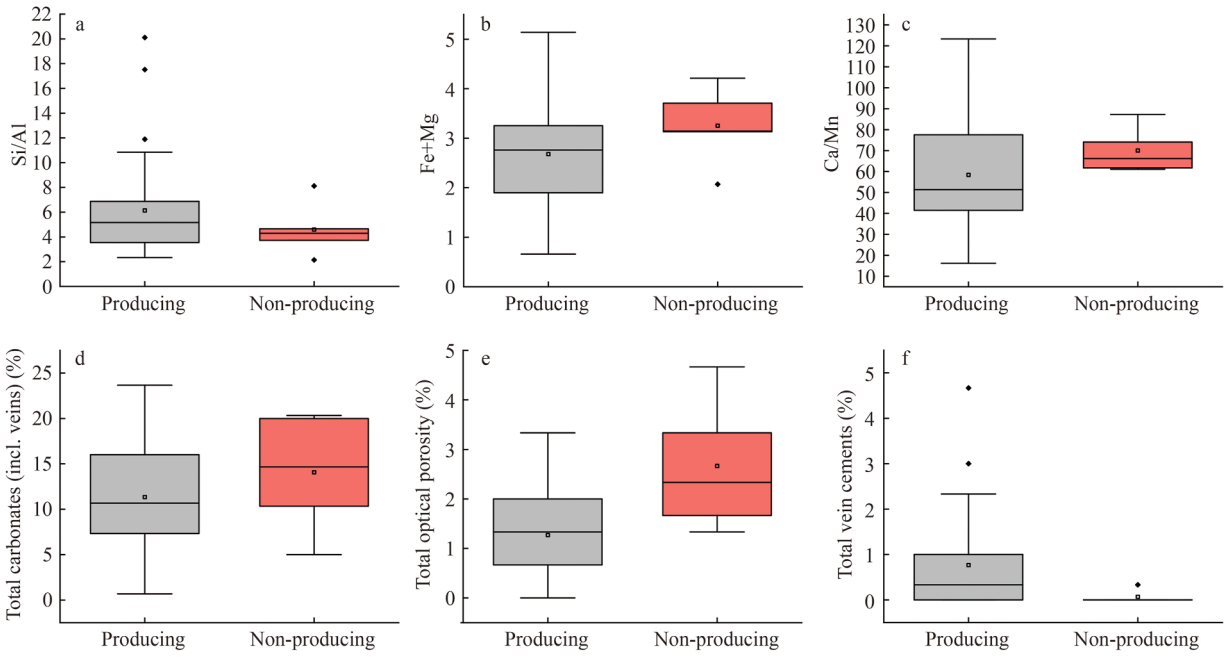

Fig. 16. Box-and-whisker bars plotted for geochemical data (a–c) derived from pXRF, and petrographic data (d–f) obtained from point counting, and producing (grey)/non-producing (red) intervals for well 1 and well 2 ($N = 42$). The producing interval has on average lower Fe + Mg content (b), lower optical porosity (e), and higher amount of total vein contents (f). But properties like Si/Al (a), Ca/Mn ratio (c), and the total carbonates including veins (d) are overlapping and cannot be used to distinguish between producing and non-producing intervals for the two wells.

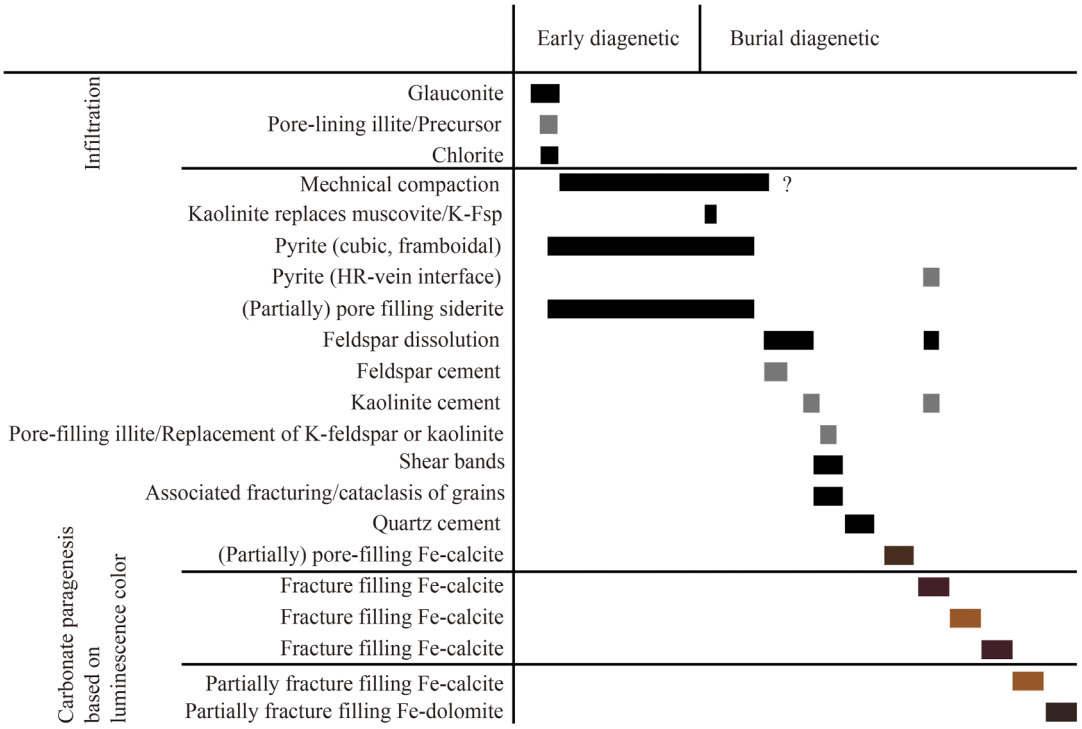

Fig. 17. Paragenetic sequence for well 1 & well 2 subdivided into relative early and burial diagenesis. The diagenetic sequence is established using transmitted light microscopy and CL analyses to differentiate vein and cement generations based on their luminescence color and texture. Black boxes mean mineral phases are found in almost all samples, grey mineral phases occur in individual samples, and the colors for Fe-calcite cement generation and veins relates to the respective CL luminescence color (non-luminescent, dull, and bright orange).

and the occurrence of grain rearrangement, cementation and/or cataclasis (Fossen et al., 2007; Ballas et al., 2013) (cf. Fig. 12). They often form in poorly consolidated, porous sand(stones) (Antonellini and Aydin, 1995; Fossen, 2010; Ballas et al., 2012; Soliva et al., 2013). As the observed shear bands in the studied wells are characterized by a reduced grain size, porosity reduction,

and grains showing an angular shape, the bands can be classified as cataclastic deformation bands. Porosity reduction due to deformation band formation is caused by crushed and small grain fragments which block pores (Antonellini and Aydin, 1994; Ballas et al., 2013), as it is also observed in this study (Fig. 12). The crushed grains may further act as precipitation sites for syntaxial quartz cements, further reducing porosity. However, the lateral continuity, which is important for the interpretation of an influence on fluid flow (Saillet and Wibberley, 2013; Busch et al., 2015), cannot be ascertained by using drill cuttings. While deformation bands may limit flow perpendicular to the deformation band, some studies suggest enhanced permeability in the plane of the deformation band (Fowles and Burley, 1994). The cataclastic deformation bands in this study are interpreted to predate the formation of quartz and carbonate cementation, as no crushed carbonate cements are obtained within the fine grained, angular and densely packed zones in the deformation bands (Fig. 12) and intragranular fractures in quartz grains are filled by syntaxial quartz cements (Fig. 13d). Furthermore, the cataclastic lenses are encased in Fe-Cal vein cements indicating shear band formation prior to vein formation (Fig. 12c). On the other hand, the artificial shear bands, only observed on the outside of cutting fragments and as individual cutting fragments, are most likely related to drilling. However, they can easily be differentiated from natural shear bands in the studied samples by high porosity in the artificial shear band and ground up pore-filling Fe-Cal cements.

Based on the luminescence color from CL analyses and the crosscutting relation of veins (Figs. 13 and 14), three pervasively-sealed vein cementation phases, and three partially-sealed carbonate vein cement generations are observed. Partially-sealed veins show euhedral crystal facets composed of orange luminescence Fe-Cal, which is brighter than the pore-filling Fe-Cal cement (Fig. 13b and c). Partially-sealed veins show an outer rim of dull luminescent Fe-Dol in all studied samples, which is interpreted to be the last generation of fracture cements. Additionally, one pervasively sealed vein shows a dissolved Fe-Cal rim. However, interpretation solely based on luminescence colors and texture cannot be considered to account for different fracture orientations as this information is not available from cutting fragments. The most prominent fracture mineralization is Fe-Cal, with minor contents of Fe-Dol forming the dull to non-luminescent outer rim in partially sealed veins (see also Hilgers and Urai, 2002; Greve et al., 2024 for further information on CL color). At the host rock-vein interface, some veins show the occurrence of pyrite (Fig. 11j). Pyrite may result from fluid-rock interactions possibly including Fe released from ongoing fluid expulsion from intercalated mudrocks (Miocic et al., 2020; Greve et al., 2024).

5.5. Reservoir quality controls and application of cutting analyses in reservoir geology

The overall poor matrix porosity of the sandstones within the two studied wells is controlled by compaction and cementation of former pore spaces predominantly by Fe-Cal. While cementation in sandstones can occasionally enhance reservoir quality by inhibiting mechanical compaction (e.g., Busch et al., 2022), further ongoing cementation reduces reservoir quality (e.g., Houseknecht, 1987; Morad, 1998; Busch et al., 2024).

Intragranular porosity is mostly present in individual K-Fsp grains and/or partially preserved if kaolinite is formed as an alteration product. The intragranular porosity is only up to 2.3 % and thus unlikely to improve permeability, as it is mostly not connected in 3D (Pittman, 1979; Kumar et al., 2023). Microporosity e.g., in chlorite, kaolinite, mudrock RF or illite is not visible in transmitted light microscopy, but could enhance the porosity in total (e.g., Nadeau and Hurst, 1991). Considering the low optical porosity (0–5 %), flow is likely restricted to open fractures and partially sealed veins rather than the matrix porosity. This observation is in line with the typical production behavior of this reservoir, which is historically characterized by high initial rates followed by a rapid decline (Möbius et al., 2023). Additionally, Sauer et al. (1992) describes that the reservoir quality of the flysch is depended on open fractures and mylonitized fracture zones (cp. cataclastic deformation bands). The observation of overall higher contents of vein cements in samples from producing intervals as opposed to non-producing intervals (Fig. 16) and including the fact that such are often only partially filling the fractures, may be a useful proxy to differentiate productive and non-productive zones. Especially partially sealed veins have been shown to preserve permeability in reservoir sandstones (e.g., Lander and Laubach, 2015 and references therein). In tight reservoirs, the understanding of fracture systems, or partially sealed veins, and their connectivity is crucial to reduce uncertainties in production (e.g., Narr, 1996; Bahrami et al., 2012; Becker et al., 2018). Future work in the Flysch play should include samples of known orientation to assess partially and completely sealed fractures in relation to the present-day stress field (e.g., Allgaier et al., 2024).

Cataclastic deformation has been described in reservoirs from the Vienna Basin (Gier et al., 2008). In the investigated samples, their formation is interpreted to predate the formation of fractures and veins (Fig. 12c). Therefore, we interpret that any compartmentalization due to deformation bands is overcome by fracturing and that production performance is linked to low matrix porosities and fracture-bound fluid flow.

For the two studied wells, producing intervals are characterized by mostly lower Fe + Mg contents (Fig. 16b) and a higher content of carbonate vein cements (Fig. 16f). As the total carbonate cement content (incl. vein cements) (Fig. 16d) is not a suitable criterion to differentiate producing and non-producing intervals, the inclusion of petrographic studies assessing vein cement contents and textures, in addition to pXRF measurements (Fig. 16b, f), is needed.

Utilizing a combined petrographic and handheld pXRF approach on cuttings in concert with historical production data may additionally enable future assessments of producing/non-producing intervals in case core material is not available. Reservoir sandstones in general cover a wide range in detrital and authigenic composition and reservoir quality controls which differ from region to region. Thus, case specific calibration of this approach is required.

Although the outlined pXRF analyses are non-destructive and petrographic analyses can still be performed on the same samples, as presented here, some other pXRF approaches require crushed sample material and calibration with a known standard (e.g., Weedmark et al., 2014). The presented approach, also utilized by Quandt et al. (2024), can be used directly on cutting and core samples and can be checked during measurements against a known standard to allow deployment at the well site in parallel to standard optical cutting analyses.

Although fracture and vein orientations cannot be reconstructed by analyzing drill cuttings, the presence of partially sealed veins and their occurrence in specific formation intervals can be identified and used for reservoir quality assessments. While porosities may be estimated based on thin sections of cuttings or standard lab measurements, direct measurements of permeability or mechanical properties are difficult using cutting material for reservoir quality assessment, a gap may be bridged by utilizing digital rocks (Monsees et al., 2020a). The inability to accurately re-orient cuttings to gain information on sediment structures and vein/fracture orientations, however, requires core- and logging

data and a structural model. Especially partially sealed veins, which may preserve open fracture porosity in the present day stress field (Laubach et al., 2004), may need to be further evaluated in these naturally fractured reservoir lithologies, and knowledge about their orientation is essential for dilation- and shear-tendency evaluations (Allgaier et al., 2023).

In cases where core material is unavailable, drill cutting analysis using petrography, pXRF, and geophysical log measurements can be a powerful tool to bridge knowledge gaps and enhance the utilization of reservoir systems worldwide.

6. Conclusion

A detailed petrographic study of sandstone drill cuttings from the Glauconite Sandstone (GLS) in the Vienna Basin highlights low optical porosity (<5 %) in samples from both wells due to cementation with mostly Fe-Cal. This study enables the assessment that fracture formation is postdating the formation of deformation bands, which enhances reservoir properties. The reservoir quality in the studied section is independent of compaction of the sandstones and is only related to fractures and partially sealed veins in sandstones with lower optical porosity, higher carbonate vein contents, and lower Fe + Mg contents from pXRF analyses.

Further geochemical data obtained from pXRF as e.g., the Si/Al-ratio to distinguish between mudrock-rich and sandstone-rich intervals, can additionally be used to cross-check formation depths of cuttings to relate them to log-derived gamma ray measurements and other well-log data. As μm-wide partially sealed veins are not visible in image logs, cuttings can additionally inform about microstructures that may influence reservoir-scale fluid migration. Furthermore, cutting examination highlights that the glauconite content in the 1. and 2. GLS is lower than that in the 3. GLS. Cuttings can thus be used to derive meaningful paragenetic sequences, assess reservoir quality controls, and deliver information about changes in the detrital mineralogy.

Due to the observed low pore volume the most critical factor contributing to reservoir quality are open fractures or partially sealed veins. Partially sealed veins preserved in cuttings, derived from petrographic analyses and pXRF measurements may thus indicate producing reservoir intervals in the low porosity reservoirs studied. This may support log-derived petrophysical interpretations in particular in the absence of core material e.g., when working on historic data sets.

CRediT authorship contribution statement

Jasemin A. Ölmez: Writing – original draft, Visualization, Methodology, Investigation. **Benjamin Busch:** Writing – review & editing, Methodology, Funding acquisition, Conceptualization. **Rolf Möbius:** Writing – review & editing, Validation, Resources. **Kanchan Dasgupta:** Writing – review & editing, Validation, Resources. **Albert L. Gauer:** Writing – review & editing, Validation. **Filippo Tosoratti:** Writing – review & editing, Validation. **Christoph Hilgers:** Writing – review & editing, Supervision, Conceptualization.

Declaration of competing interest

The authors declare that they have no known competing financial interests or personal relationships that could have appeared to influence the work reported in this paper.

Acknowledgements

JÖ, BB, and CH thank OMV Exploration & Production GmbH for providing research funding, access to sample material, and permission to publish the data. Martin von Dollen is thankfully acknowledged for thin section preparation. The authors thankfully acknowledge constructive review comments by anonymous reviewers and editorial handling by Dr. Radwan and Dr. Yang.

Appendix A. Supplementary data

Supplementary data to this article can be found online at https://doi.org/10.1016/j.engeos.2025.100461.

References

Adamolekun, O.J., Busch, B., Suess, M.P., Molenaar, N., Hilgers, C., 2022. Petrography and reservoir quality controls in shallow transitional marine Cretaceous-Paleogene deposits in the Dahomey Basin, Nigeria. J. Afr. Earth Sci. 186, 104437. https://doi.org/10.1016/j.jafrearsci.2021.104437.

Allgaier, F., Busch, B., Niederhuber, T., Quandt, D., Müller, B., Hilgers, C., 2023. Fracture network characterisation of the naturally fractured Upper Carboniferous sandstones combining outcrop and wellbore data, Ruhr Basin, Germany. Z. Dtsch. Ges. Geowiss. 173 (4), 599–623. https://doi.org/10.1127/zdgg/2023/0369.

Allgaier, F., Niederhuber, T., Busch, B., Müller, B., Hilgers, C., 2024. Post-mining related reactivation potential of faults hosted in tight reservoir rocks around flooded coal mines, eastern Ruhr Basin, Germany. Geomechanics for Energy and the Environment 38, 100560. https://doi.org/10.1016/j.gete.2024.100560.

Amorosi, A., 2013. The occurrence of glaucony in the stratigraphic record: distribution patterns and sequence-stratigraphic significance. Linking Diagenesis to Sequence Stratigraphy 37–53. https://doi.org/10.1002/9781118485347.ch2.

Antonellini, M., Aydin, A., 1994. Effect of faulting on fluid flow in porous sandstones: petrophysical properties 1. AAPG (Am. Assoc. Pet. Geol.) Bull. 78 (3), 355–377. https://doi.org/10.1306/bdff90aa-1718-11d7-8645000102c1865d.

Antonellini, M., Aydin, A., 1995. Effect of faulting on fluid flow in porous sandstones: geometry and spatial distribution. AAPG (Am. Assoc. Pet. Geol.) Bull. 79, 642–671.

Arzmüller, G., Buchta, Š., Ralbovský, E., Wessely, G., Golonka, J., Picha, F.J., 2006. The Vienna Basin, the Carpathians and Their Foreland: Geology and Hydrocarbon Resources. American Association of Petroleum Geologists, pp. 191–204. https://doi.org/10.1306/985608m843068.

Bahrami, H., Rezaee, R., Hossain, M., 2012. Characterizing natural fractures productivity in tight gas reservoirs. J. Pet. Explor. Prod. Technol. 2 (2), 107–115. https://doi.org/10.1007/s13202-012-0026-x.

Baioumy, H., Farouk, S., Al-Kahtany, K., 2020. Paleogeographic, paleoclimatic and sea-level implications of glauconite deposits in Egypt: a review. J. Afr. Earth Sci. 171, 103944. https://doi.org/10.1016/j.jafrearsci.2020.103944.

Ballas, G., Soliva, R., Sizun, J.-P., Benedicto, A., Cavailhes, T., Raynaud, S., 2012. The importance of the degree of cataclasis in shear bands for fluid flow in porous sandstone, Provence, France. AAPG (Am. Assoc. Pet. Geol.) Bull. 96 (11), 2167–2186. https://doi.org/10.1306/04051211097.

Ballas, G., Soliva, R., Sizun, J.-P., Fossen, H., Benedicto, A., Skurtveit, E., 2013. Shear-enhanced compaction bands formed at shallow burial conditions; implications for fluid flow (Provence, France). J. Struct. Geol. 47, 3–15. https://doi.org/10.1016/j.jsg.2012.11.008.

Beard, D.C., Weyl, P.K., 1973. Influence of texture on porosity and permeability of unconsolidated sand 1. AAPG (Am. Assoc. Pet. Geol.) Bull. 57 (2), 349–369. https://doi.org/10.1306/819a4272-16c5-11d7-8645000102c1865d.

Becker, I., Koehrer, B., Waldvogel, M., Jelinek, W., Hilgers, C., 2018. Comparing fracture statistics from outcrop and reservoir data using conventional manual and t-LiDAR derived scanlines in Ca2 carbonates from the Southern Permian Basin, Germany. Mar. Petrol. Geol. 95, 228–245. https://doi.org/10.1016/j.marpetgeo.2018.04.021.

Berka, R., 2015. Zur Geologie der großen Beckengebiete des Ostalpenraumes. Abh. Geol. Bundesanst. 64, 71–141.

Berner, R.A., 1970. Sedimentary pyrite formation. Am. J. Sci. 268 (1), 1–23. https://doi.org/10.2475/ajs.268.1.1.

Bjørlykke, K., 1988. Chapter 2 sandstone diagenesis in relation to preservation, destruction and creation of porosity. In: Chilingarian, G.V., Wolf, K.H. (Eds.), Diagenesis, I. Elsevier, pp. 555–588. https://doi.org/10.1016/S0070-4571(08)70180-8.

Bjørlykke, K., Egeberg, P.K., 1993. Quartz cementation in sedimentary basins 1. AAPG (Am. Assoc. Pet. Geol.) Bull. 77 (9), 1538–1548. https://doi.org/10.1306/bdff8ee8-1718-11d7-8645000102c1865d.

Bjørrlykke, K., 1998. Clay mineral diagenesis in sedimentary basins; a key to the prediction of rock properties; examples from the North Sea Basin. Clay Miner. 33 (1), 15–34.

Budd, D.A., Hammes, U., Ward, W.B., 2000. Cathodoluminescence in calcite cements new insights on Pb and Zn sensitizing, Mn activation, and Fe quenching

at low trace-element concentrations. J. Sediment. Res. 70, 217–226. https://doi.org/10.1306/2DC4090C-0E47-11D7-8643000102C1865D.
Busch, B., Adelmann, D., Herrmann, R., Hilgers, C., 2022. Controls on compactional behavior and reservoir quality in a triassic buntsandstein reservoir, upper rhine graben, SW Germany. Mar. Petrol. Geol. 136, 105437. https://doi.org/10.1016/j.marpetgeo.2021.105437.
Busch, B., Böcker, J., Hilgers, C., 2024. Improved reservoir quality assessment by evaluating illite grain coatings, quartz cementation, and compaction–case study from the Buntsandstein, Upper Rhine Graben. Germany Geoenergy Science and Engineering 241, 213141. https://doi.org/10.1016/j.geoen.2024.213141.
Busch, B., Hilgers, C., Lander, R.H., Bonnell, L.M., Adelmann, D., 2018. Reservoir quality and burial model evaluation by kinetic quartz and illite cementation modeling: case study of Rotliegendes, north Germany. AAPG (Am. Assoc. Pet. Geol.) Bull. 102 (2), 293–307. https://doi.org/10.1306/0503171605217075.
Busch, B., Winkler, R., Osivandi, K., Nover, G., Amann, A., Hilgers, C., 2015. Evolution of Small-Scale Flow Barriers in German Rotliegend Siliciclastics, vol. 435. Geological Society London Special Publications. https://doi.org/10.1144/SP435.3.
Caja, M.A., Santos, C., García, L., Fernandez, P.R., Pérez, J.L., Peña, A., Canal, J., Blázquez, V., González, H., Sánchez, V., García, A.J., 2019. Characterizing Algeria tight reservoir cutting samples with virtual microscopy, petrography, mineralogy and digital petrophysics. EAGE/ALNAFT Geoscience Workshop 2019. EAGE, Algiers, Africa.
Camp, E.R., Jordan, T.E., Hornbach, M.J., Whealton, C.A., 2018. A probabilistic application of oil and gas data for exploration stage geothermal reservoir assessment in the Appalachian Basin. Geothermics 71, 187–199. https://doi.org/10.1016/j.geothermics.2017.09.001.
Ciriaco, A.E., Zarrouk, S.J., Zakeri, G., 2020. Geothermal resource and reserve assessment methodology: overview, analysis and future directions. Renew. Sustain. Energy Rev. 119, 109515. https://doi.org/10.1016/j.rser.2019.109515.
Cohen, K.M., Harper, D.A.T., Gibbard, P.L., 2024. ICS International Chronostratigraphic Chart 2024/12. International Commission on Stratigraphy IUGS.
Coleman, M.L., 1985. Geochemistry of diagenetic, non-silicate minerals: kinetic considerations. Phil. Trans. Roy. Soc. Lond. Math. Phys. Sci. 315, 39–56. https://doi.org/10.1098/rsta.1985.0028.
Coskun, S.B., Wardlaw, N.C., Haverslew, B., 1993. Effects of composition, texture and diagenesis on porosity, permeability and oil recovery in a sandstone reservoir. J. Petrol. Sci. Eng. 8 (4), 279–292. https://doi.org/10.1016/0920-4105(93)90005-Y.
Craigie, N., 2018. Principles of Elemental Chemostratigraphy - A Practical User Guide. Springer, Cham, p. 189. https://doi.org/10.1007/978-3-319-71216-1.
Cummins, W.A., 1962. The greywacke problem. Geol. J. 3 (1), 51–72. https://doi.org/10.1002/gj.3350030105.
Decker, K., 1996. Miocene tectonics at the Alpine-Carpathian junction and the evolution of the Vienna Basin. Mitt. Ges. Geol. Bergbaustud. Osterr. 41, 33–44.
Decker, K., Peresson, H., Hinsch, R., 2005. Active tectonics and Quaternary basin formation along the Vienna Basin transform fault. Quat. Sci. Rev. 24 (3), 305–320. https://doi.org/10.1016/j.quascirev.2004.04.012.
Demars, C., Pagel, M., Deloule, E., Blanc, P., 1996. Cathodoluminescence of quartz from sandstones: interpretation of the UV range by determination of trace element distributions and fluid-inclusion P-T-X properties in authigenic quartz. Am. Mineral. 81 (7–8), 891–901. https://doi.org/10.2138/am-1996-7-812.
Dickinson, W.R., Suczek, C.A., 1979. Plate tectonics and sandstone compositions 1. AAPG (Am. Assoc. Pet. Geol.) Bull. 63 (12), 2164–2182. https://doi.org/10.1306/2f9188fb-16ce-11d7-8645000102c1865d.
Dickson, J.A.D., 1965. A modified staining technique for carbonates in thin section. Nature 205 (4971), 587. https://doi.org/10.1038/205587a0.
Dutton, S.P., Loucks, R.G., 2010. Diagenetic controls on evolution of porosity and permeability in lower Tertiary Wilcox sandstones from shallow to ultradeep (200–6700m) burial, Gulf of Mexico Basin, U.S.A. Mar. Petrol. Geol. 27 (1), 69–81. https://doi.org/10.1016/j.marpetgeo.2009.08.008.
Fernández-Ibáñez, F., DeGraff, J.M., Ibrayev, F., 2018. Integrating borehole image logs with core: A method to enhance subsurface fracture characterization. AAPG (Am. Assoc. Pet. Geol.) Bull. 102 (6), 1067–1090. https://doi.org/10.1306/0726171609317002.
Folk, R.L., 1980. Petrology of Sedimentary Rocks. Hemphill publishing company, Austin, Texas.
Folk, R.L., Ward, W.C., 1957. Brazos River bar (Texas): A study in the significance of grain size parameters. J. Sediment. Res. 27 (1), 3–26. https://doi.org/10.1306/74d70646-2b21-11d7-8648000102c1865d.
Fossen, H., 2010. Deformation bands formed during soft-sediment deformation: Observations from SE Utah. Mar. Petrol. Geol. 27 (1), 215–222. https://doi.org/10.1016/j.marpetgeo.2009.06.005.
Fossen, H., Schultz, R., Shipton, Z., Mair, K., 2007. Deformation bands in sandstone: A review. J. Geol. Soc. 164. https://doi.org/10.1144/0016-76492006-036.
Fowles, J., Burley, S., 1994. Textural and permeability characteristics of faulted, high porosity sandstones. Mar. Petrol. Geol. 11 (5), 608–623. https://doi.org/10.1016/0264-8172(94)90071-X.
Gier, S., Worden, R.H., Johns, W.D., Kurzweil, H., 2008. Diagenesis and reservoir quality of Miocene sandstones in the Vienna Basin, Austria. Mar. Petrol. Geol. 25 (8), 681–695. https://doi.org/10.1016/j.marpetgeo.2008.06.001.
Gier, S., Worden, R.H., Krois, P., 2018. Comparing clay mineral diagenesis in interbedded sandstones and mudstones, Vienna Basin, Austria. Geological Society, London, Special Publications 435 (1), 389–403. https://doi.org/10.1144/SP435.9.
Götze, J., Plötze, M., Habermann, D., 2001. Origin, spectral characteristics and practical applications of the cathodoluminescence (CL) of quartz–a review. Mineral. Petrol. 71 (3), 225–250. https://doi.org/10.1007/s007100170040.
Götzinger, H.G., Grill, R., Küpper, H., Lichtenberger, E., Rosenberg, G., 1954. Erläuterungen zur geologischen Karte der Umgebung von Wien 1:75.000. Geologische Bundesanstalt Wien, Wien.
Greve, J., Busch, B., Quandt, D., Knaak, M., Hilgers, C., 2024. The influence of sedimentary facies, mineralogy, and diagenesis on reservoir properties of the coal-bearing Upper Carboniferous of NW Germany. Pet. Geosci. 30 (1). https://doi.org/10.1144/petgeo2023-020 petgeo2023-2020.
Griffiths, J., Worden, R.H., Wooldridge, L.J., Utley, J.E.P., Duller, R.A., 2019. Compositional variation in modern estuarine sands: Predicting major controls on sandstone reservoir quality. AAPG (Am. Assoc. Pet. Geol.) Bull. 103 (4), 797–833. https://doi.org/10.1306/09181818025.
Harzhauser, M., Kranner, M., Mandic, O., Strauss, P., Siedl, W., Piller, W., 2020. Miocene lithostratigraphy of the northern and central Vienna Basin (Austria). Austrian Journal of Earth Sciences 113, 169–199. https://doi.org/10.17738/ajes.2020.0011.
Hilgers, C., Urai, J.L., 2002. Microstructural observations on natural syntectonic fibrous veins: implications for the growth process. Tectonophysics 352 (3–4), 257–274. https://doi.org/10.1016/S0040-1951(02)00185-3.
Houseknecht, D.W., 1987. Assessing the relative importance of compaction processes and cementation to reduction of porosity in sandstones 1. AAPG (Am. Assoc. Pet. Geol.) Bull. 71 (6), 633–642. https://doi.org/10.1306/9488787f-1704-11d7-8645000102c1865d.
Ibrahem, Y., Morozov, V.P., 2024. Exploring the potential of drill cuttings for reservoir characterization: A case study from the Volga-Ural basin, Russia. Petroleum Research. https://doi.org/10.1016/j.ptlrs.2024.01.012.
Johan, B.S., Neil, R.H., 2001. Comparison between outcrop-spectral gamma ray logging and whole rock geochemistry: Implications for quantitative reservoir characterisation in continental sequences. Mar. Petrol. Geol. 18 (6), 657–670. https://doi.org/10.1016/S0264-8172(01)00022-8.
Khelifa, C., Zeddouri, A., Djabes, F., 2014. Influence of natural fractures on oil production of unconventional reservoirs. Energy Proc. 50, 360–367. https://doi.org/10.1016/j.egypro.2014.06.043.
Knox, J.A., Ripley, H.E., 1979. Fracture acidizing in carbonate rock. J. Can. Petrol. Technol. 18, 4. https://doi.org/10.2118/79-04-07.
Kumar, A., Prajapati, N., Späth, M., Busch, B., Schneider, D., Hilgers, C., Nestler, B., 2023. Qualitative dissolution modeling of etch-pit formation on the K-feldspar surface through phase-field approach. J. Geophys. Res. Solid Earth 128 (4), e2022JB025749. https://doi.org/10.1029/2022JB025749.
Ladwein, H.W., 1988. Organic geochemistry of Vienna Basin: Model for hydrocarbon generation in overthrust belts 1. AAPG (Am. Assoc. Pet. Geol.) Bull. 72 (5), 586–599. https://doi.org/10.1306/703c8ed4-1707-11d7-8645000102c1865d.
Lamarche, J., Lavenu, A.P.C., Gauthier, B.D.M., Guglielmi, Y., Jayet, O., 2012. Relationships between fracture patterns, geodynamics and mechanical stratigraphy in carbonates (South-East Basin, France). Tectonophysics 581, 231–245. https://doi.org/10.1016/j.tecto.2012.06.042.
Lander, R.H., Larese, R.E., Bonnell, L.M., 2008. Toward more accurate quartz cement models: The importance of euhedral versus noneuhedral growth rates. AAPG (Am. Assoc. Pet. Geol.) Bull. 92 (11), 1537–1563. https://doi.org/10.1306/07160808037.
Lander, R.H., Laubach, S.E., 2015. Insights into rates of fracture growth and sealing from a model for quartz cementation in fractured sandstones. GSA Bulletin 127 (3–4), 516–538. https://doi.org/10.1130/b31092.1.
Lanson, B., Beaufort, D., Berger, G., Bauer, A., Cassagnabère, A., Meunier, A., 2002. Authigenic kaolin and illitic minerals during burial diagenesis of sandstones: A review. Clay Miner. 37 (1), 1–22. https://doi.org/10.1180/0009855023710014.
Laubach, S.E., Olson, J.E., Gale, J.F.W., 2004. Are open fractures necessarily aligned with maximum horizontal stress? Earth Planet Sci. Lett. 222 (1), 191–195. https://doi.org/10.1016/j.epsl.2004.02.019.
López-Quirós, A., Sánchez-Navas, A., Nieto, F., Escutia, C., 2020. New insights into the nature of glauconite. Am. Mineral. 105, 674–686. https://doi.org/10.2138/am-2020-7341.
Lupin, J.H., Hampson, G.J., 2020. Sediment-routing controls on sandstone bulk petrographic composition and texture across an ancient shelf: Example from Cretaceous Western Interior Basin, Utah and Colorado. U.S.A. Journal of Sedimentary Research 90 (10), 1389–1409. https://doi.org/10.2110/jsr.2020.044.
Makowitz, A., Lander, R., Milliken, K., 2006. Diagenetic modeling to assess the relative timing of quartz cementation and brittle grain processes during compaction. AAPG (Am. Assoc. Pet. Geol.) Bull. 90, 873–885. https://doi.org/10.1306/12190505044.
Mamdouh, M., Reda, M., Raef, A., El Din, M.Y.Z., Abdelhafeez, T.H., Al-Hashim, M.H., 2024. Reservoir quality, lithotype assessment, and geochemical source rock analysis: insights from well logs and pyrolysis data, Karama Field, North-Western Desert, Egypt. Geofluids 1, 1235792. https://doi.org/10.1155/2024/1235792, 2024.
Mattern, F., Wang, P.J., 2008. Out-of-sequence thrusts and paleogeography of the Rhenodanubian Flysch Belt (Eastern Alps) revisited. Int. J. Earth Sci. 97 (4), 821–833. https://doi.org/10.1007/s00531-007-0200-4.
Mauriohooho, K., Barker, S.L.L., Rae, A., 2016. Mapping lithology and hydrothermal alteration in geothermal systems using portable X-ray fluorescence (pXRF): A case study from the Tauhara geothermal system, Taupo Volcanic Zone. Geothermics 64, 125–134. https://doi.org/10.1016/j.geothermics.2016.03.005.

Milton, N.J., Emery, D., 1996. Outcrop and well data. In: Emery, D., Myers, K.J. (Eds.), Sequence Stratigraphy. BP Exploration, Stockley Park, Uxbridge, London, pp. 61–79.
Miocic, J.M., Girard, J.-P., Schöner, R., Gaupp, R., 2020. Mudstone/sandstone ratio control on carbonate cementation and reservoir quality in Upper Permian Rotliegend sandstones, offshore the Netherlands. Mar. Petrol. Geol. 115. https://doi.org/10.1016/j.marpetgeo.2020.104293.
Möbius, R., Gauer, A., Tosoratti, F., 2023. Exploring for unlocked subsurface potential by integration of historic and modern data: The case of a forgotten Flysch reservoir within the Vienna Basin (Austria) discovered almost a century ago, DGMK/ÖGEW Frühjahrstagung 2023, Celle (Germany), 157-160.
Molenaar, N., 1986. The interrelation between clay infiltration, quartz cementation, and compaction in lower Givetian terrestrial sandstones, northern Ardennes, Belgium. J. Sediment. Res. 56 (3), 359–369. https://doi.org/10.1306/212f8913-2b24-11d7-8648000102c1865d.
Monsees, A., Subhedar, A., Busch, B., Nestler, B., Hilgers, C., 2020a. Calibrating micro-computed tomography data to permeability experiments and petrography - insights from Digital Rocks. Oil Gas Eur. Mag. 28–33. https://doi.org/10.19225/200908.
Monsees, A.C., Busch, B., Schöner, N., Hilgers, C., 2020b. Rock typing of diagenetically induced heterogeneities–A case study from a deeply-buried clastic Rotliegend reservoir of the Northern German Basin. Mar. Petrol. Geol. 113, 104163. https://doi.org/10.1016/j.marpetgeo.2019.104163.
Morad, S., 1998. Carbonate Cementation in Sandstones: Distribution Patterns and Geochemical Evolution. In: Morad, S. (Ed.), Carbonate Cementation in Sandstones: Distribution Patterns and Geochemical Evolution. Blackwell Science Ltd, Oxford, UK, pp. 1–26.
Morad, S., Al-Ramadan, K., Ketzer, J.M., De Ros, L.F., 2010. The impact of diagenesis on the heterogeneity of sandstone reservoirs: A review of the role of depositional facies and sequence stratigraphy. AAPG (Am. Assoc. Pet. Geol.) Bull. 94 (8), 1267–1309. https://doi.org/10.1306/04211009178.
Morad, S., Ketzer, M., De Ros, L., 2002. Spatial and temporal distribution of diagenetic alterations in siliclastic rocks: Implications for mass transfer in sedimentary basins. Sedimentology 47, 95–120. https://doi.org/10.1046/j.1365-3091.2000.00007.x.
Nadeau, P.H., Hurst, A., 1991. Application of back-scattered electron microscopy to the quantification of clay mineral microporosity in sandstones. J. Sediment. Res. 61 (6), 921–925. https://doi.org/10.1306/d4267807-2b26-11d7-8648000102c1865d.
Narr, W., 1996. Estimating average fracture spacing in subsurface rock 1. AAPG (Am. Assoc. Pet. Geol.) Bull. 80 (10), 1565–1585. https://doi.org/10.1306/64eda0b4-1724-11d7-8645000102c1865d.
Odin, G.S., Fullagar, P.D., 1988. Chapter C4 Geological significance of the glaucony facies. Green Marine Clays. Elsevier, pp. 295–332. https://doi.org/10.1016/S0070-4571(08)70069-4.
Offshore, 2021. Norwegian Trio Develop Drill Cuttings Digital Visualization Tool. https://www.offshore-mag.com/geosciences/article/14206534/norwegian-trio-develop-drill-cuttings-digital-visualization-tool. (Accessed 15 August 2025).
Olson, J.E., Laubach, S.E., Lander, R.H., 2009. Natural fracture characterization in tight gas sandstones: Integrating mechanics and diagenesis. AAPG (Am. Assoc. Pet. Geol.) Bull. 93 (11), 1535–1549. https://doi.org/10.1306/08110909100.
Ozkan, A., Cumella, S.P., Milliken, K.L., Laubach, S.E., 2011. Prediction of lithofacies and reservoir quality using well logs, Late Cretaceous Williams Fork Formation, Mamm Creek field, Piceance Basin, Colorado. AAPG (Am. Assoc. Pet. Geol.) Bull. 95 (10), 1699–1723. https://doi.org/10.1306/01191109143.
Paxton, S.T., Szabo, J.O., Ajdukiewicz, J.M., Klimentidis, R.E., 2002. Construction of an intergranular volume compaction curve for evaluating and predicting compaction and porosity loss in rigid-grain sandstone reservoirs. AAPG (Am. Assoc. Pet. Geol.) Bull. 86 (12), 2047–2067. https://doi.org/10.1306/61eeddfa-173e-11d7-8645000102c1865d.
Piller, W.E., Decker, K., Haas, M., 1996. Sedimentologie und Beckendynamik des Wiener Beckens. Exursionsführer SEDIMENT 96, 41.
Pittman, E.D., 1979. Porosity, diagenesis and productive capability of sandstone reservoirs. In: Scholle, P.A., Schluger, P.R. (Eds.), Aspects of Diagenesis. SEPM Society for Sedimentary Geology. https://doi.org/10.2110/pec.79.26.0159.
Quandt, D., Busch, B., Greve, J., Hilgers, C., 2024. Rock characteristics and reservoir properties of Upper Carboniferous (Stephanian A–B) tight siliciclastic rocks from the Saar–Nahe basin (SW Germany). Int. J. Earth Sci. https://doi.org/10.1007/s00531-024-02394-x.
Radwan, A.E., 2022. Provenance, depositional facies, and diagenesis controls on reservoir characteristics of the middle Miocene Tidal sandstones, Gulf of Suez Rift Basin: integration of petrographic analysis and gamma-ray log patterns. Environ. Earth Sci. 81 (15). https://doi.org/10.1007/s12665-022-10502-w.
Rammel, M., 1989. Zur Kenntnis der Flyschzone im Untergrund des Wiener Beckens - Die Glaukonitsandsteinserie. Universität Wien, p. 152.
Rider, M., Kennedy, M., 2011. The Geological Interpretation of Well Logs, third ed. Rider-French Consulting Ltd., Scotland, p. 432.
Rider, M.H., 1990. Gamma-ray Log Shape Used as a Facies Indicator: Critical Analysis of an Oversimplified Methodology, 48. Geological Society Special Publication, pp. 27–37. https://doi.org/10.1144/GSL.SP.1990.048.01.04.
Rossi, C., Alaminos, A., 2014. Evaluating the mechanical compaction of quartzarenites: The importance of sorting (Llanos foreland basin, Colombia). Mar. Petrol. Geol. 56, 222–238. https://doi.org/10.1016/j.marpetgeo.2014.04.012.
Royden, L.H., Biddle, K.T., Christie-Blick, N., 1985. The Vienna Basin: A thin-skinned pull-apart basin, Strike-Slip Deformation. Basin Formation, and Sedimentation. SEPM Society for Sedimentary Geology. https://doi.org/10.2110/pec.85.37.0303.
Rupprecht, B.J., 2017. Hydrocarbon generation and alteration in the Vienna Basin. PhD thesis, Montan Universität Leoben, p. 295.
Rupprecht, B.J., Sachsenhofer, R.F., Gawlick, H.J., Kallanxhi, M.E., Kucher, F., 2017. Jurassic source rocks in the Vienna Basin (Austria): Assessment of conventional and unconventional petroleum potential. Mar. Petrol. Geol. 86, 1327–1356. https://doi.org/10.1016/j.marpetgeo.2017.07.026.
Rupprecht, B.J., Sachsenhofer, R.F., Zach, C., Bechtel, A., Gratzer, R., Kucher, F., 2018. Oil and gas in the Vienna Basin: Hydrocarbon generation and alteration in a classical hydrocarbon province. Pet. Geosci. 25 (1), 3–29. https://doi.org/10.1144/petgeo2017-056.
Sachsenhofer, R.F., Misch, D., Rainer, T., Rupprecht, B.J., Siedl, W., 2025. The Vienna Basin: petroleum systems, storage and geothermal potential. Geological Society, London, Special Publications 555 (1). https://doi.org/10.1144/SP555-2023-205. SP555-2023-2205.
Saillet, E., Wibberley, C., 2013. Permeability and flow impact of faults and deformation bands in high-porosity sand reservoirs: Southeast Basin, France, analog. AAPG (Am. Assoc. Pet. Geol.) Bull. 97, 437–464. https://doi.org/10.1306/09071211191.
Sanei, H., Ardakani, O.H., Akai, T., Akihisa, K., Jiang, C., Wood, J.M., 2020. Core versus cuttings samples for geochemical and petrophysical analysis of unconventional reservoir rocks. Sci. Rep. 10 (1), 7920. https://doi.org/10.1038/s41598-020-64936-y.
Santanu, B., Udita, B., Anup, 2016. A review on palaeogeographic implications and temporal variation in glaucony composition. J. Palaeogeogr. 5 (1), 43–71. https://doi.org/10.1016/j.jop.2015.12.001.
Sauer, R., Seifert, P., Wessely, G., 1992. Outline of sedimentation, tectonic framework and hydrocarbon occurrence in Eastern Lower Austria (Guidebook). Mittl. Osterreichischen Geol. Ges. 5–264.
Schicker, A., Gier, S., Schieber, J., Krois, P., 2021. Diagenesis of the Malmian Mikulov Formation source rock, Vienna Basin: Focus on matrix and pores. Mar. Petrol. Geol. 129, 105082. https://doi.org/10.1016/j.marpetgeo.2021.105082.
Schulz, H.-M., Horsfield, B., Sachsenhofer, R.F., 2010. Shale gas in Europe: A regional overview and current research activities. Geological Society, London, Petroleum Geology Conference Series 7 (1), 1079–1085. https://doi.org/10.1144/0071079.
Soliva, R., Schultz, R.A., Ballas, G., Taboada, A., Wibberley, C., Saillet, E., Benedicto, A., 2013. A model of strain localization in porous sandstone as a function of tectonic setting, burial and material properties; new insight from Provence (southern France). J. Struct. Geol. 49, 50–63. https://doi.org/10.1016/j.jsg.2012.11.011.
Sotak, J., 2010. Paleoenvironmental changes across the Eocene-Oligocene boundary: Insights from the Central-Carpathian Paleogene Basin. Geol. Carpathica 61, 393–418. https://doi.org/10.2478/v10096-010-0024-1.
Strauss, P., Harzhauser, M., Hinsch, R., Wagreich, M., 2006. Sequence stratigraphy in a classic pull-apart basin (Neogene, Vienna Basin). A 3D seismic based integrated approach. Geol. Carpathica 57 (3), 185–197.
Swami, V., Didenko, A., Allo, F., Rogers, G., Cowgill, M., Rahbi, K., Harthi, R., Verma, S.K., Zonjee, P., 2022. New insights into wellbore stability analysis with integration of petrophysics, rock physics geology, geomechanics and drilling , in: 83rd EAGE Annual Conference & Exhibition, Madrid, Spain. 1–5.
Terzaghi, R.D., 1965. Sources of error in joint surveys. Geotechnique 15 (3), 287–304. https://doi.org/10.1680/geot.1965.15.3.287.
Tiainen, S., King, H., Cubitt, C., Karalaus, E., Prater, T., Willis, B., 2002. Drill cuttings analysis & a new approach to reservoir description and characterisation; Examples from the Cooper Basin, Australia. The APPEA Journal 42 (1), 495–509. https://doi.org/10.1071/AJ01027.
Traineau, H., Genter, A., Jp, C., H, F., P, C., 1991. Petrography of the granite massif from drill cutting analysis and well log interpretation in the HDR borehole GPK1 (Soultz, Alsace, France). Geoth. Sci. Technol. 3, 1–29.
Tribovillard, N., Bout-Roumazeilles, V., Abraham, R., Ventalon, S., Delattre, M., Baudin, F., 2023. The contrasting origins of glauconite in the shallow marine environment highlight this mineral as a marker of paleoenvironmental conditions. C. R. Geosci. 355 (S2), 1–16. https://doi.org/10.5802/crgeos.170.
Triplehorn, D.M., 1966. Morphology, internal structure, and origin of glauconite pellets. Sedimentology 6 (4), 247–266. https://doi.org/10.1111/j.1365-3091.1966.tb01894.x.
Wagreich, M., Schmid, H.P., 2002. Backstripping dip-slip fault histories: Apparent slip rates for the Miocene of the Vienna Basin. Terra Nova 14 (3), 163–168. https://doi.org/10.1046/j.1365-3121.2002.00404.x.
Walderhaug, O., 2000. Modeling quartz cementation and porosity in Middle Jurassic Brent Group sandstones of the Kvitebjørn Field, Northern North Sea. AAPG Bulletin - AAPG BULL 84. https://doi.org/10.1306/A9673E96-1738-11D7-8645000102C1865D.
Weedmark, T.C., Spencer, R.J., Juss, D.P., Marecha, F., 2014. Applications of Portable XRF, Chemical Stratigraphy and SEM in the Horn River Basin, Adapted from Extended Abstract Prepared in Conjunction with Presentation at CSPG/CSEG/CWLS GeoConvention 2012, (Vision) Calgary TELUS Convention Centre & ERCB Core Research Centre, Calgary, AB, Canada, 14-18 May 2012. AAPG.
Wentworth, C.K., 1922. A scale of grade and class terms for clastic sediments. J. Geol. 30 (5), 377–392.
Wessely, G., 2006. Niederösterreich. Geologische Bundesanstalt, Wien, p. 175.
Wilmsen, M., Bansal, U., Metzner, N., Böning, P., 2024. Geochemical and depositional environment of an Upper Cretaceous greensand giant (Münsterland

Cretaceous Basin, Germany). Chem. Geol. 661, 122168. https://doi.org/10.1016/j.chemgeo.2024.122168.
Wilson, M.D., Stanton, P.T., Wilson, M.D., 1994. Diagenetic mechanisms of porosity and permeability reduction and enhancement. Reservoir Quality Assessment and Prediction in Clastic Rocks. SEPM Society for Sedimentary Geology. https://doi.org/10.2110/scn.94.30.0059.
Worden, R., Armitage, P., Butcher, A., Churchill, J., Csoma, A., Hollis, C., Lander, R., Omma, J., 2018. Petroleum Reservoir Quality Prediction: Overview and Contrasting Approaches from Sandstone and Carbonate Communities, vol. 435. Geological Society, London, Special Publications, p. SP435.421. https://doi.org/10.1144/SP435.21.
Worden, R., Morad, S., 2003. Clay Minerals in Sandstones: Controls on Formation, Distribution and Evolution, pp. 1–41. https://doi.org/10.1002/9781444304336.ch1.
Zambito, J.J., Haas, L.D., Parsen, M.J., 2022. A portable x-ray fluorescence (pXRF) elemental dataset collected from Cambrian-age sandstone aquifer material, Wisconsin, U.S.A. Data Brief 43, 108411. https://doi.org/10.1016/j.dib.2022.108411.